

Fully-coupled hydrologic processes for modeling landscape evolution



Yu Zhang ^{a,*}, Rudy Slingerland ^b, Christopher Duffy ^a

^a Department of Civil and Environmental Engineering, Pennsylvania State University, University Park, 16802, USA

^b Department of Geosciences, Pennsylvania State University, University Park, 16802, USA

ARTICLE INFO

Article history:

Received 25 June 2015

Received in revised form

21 March 2016

Accepted 13 April 2016

Keywords:

Landscape evolution

Groundwater sapping

Subsurface hydrology

Sediment transport

Morphological acceleration

LE-PIHM

ABSTRACT

Although current landscape evolution models can predict landscapes with specific concave-convex slopes, regolith thicknesses, drainage densities and relief, these models rarely include realistic groundwater and overland flows, and channel-hillslope interactions. To overcome the potential drawbacks, this study couples hydrologic processes with hillslope and channel sediment transport processes to form a new hydrologic-morphodynamic model (LE-PIHM) for regolith formation and landscape evolution. Two scenarios with and without groundwater flow are presented to demonstrate the importance of this coupling. Comparison of the steady state landforms indicates that hillslopes are steeper and relief is higher with groundwater flow. The sensitivity of the solution to mesh geometry is tested and it is shown that model simulations maintain the characteristic features of a landscape over a reasonable range of maximum area and minimum interior angle. To predict long-term landscape change, a morphological acceleration technique is presented and a method for choosing an optimal morphological scale factor is introduced.

© 2016 Elsevier Ltd. All rights reserved.

1. Introduction

Landscape evolution models (LEMs) aim to quantitatively predict the evolution of landscapes and their detailed spatial characteristics. In general LEMs are based on solving a system of equations for the continuity of mass, geomorphic transport functions that describe the generation and movement of sediment and (to a lesser extent) solutes on hillslopes, a representation of runoff generation and the routing of water across the landscape, geomorphic transport functions for erosion and transport of water-sediment mixtures in channels, and rock particle motions due to tectonics (for a review see Coulthard, 2001; Tucker and Hancock, 2010). Under relatively constant forcing, these models predict landscapes with specific concave-convex slopes and spatially variable regolith thicknesses, drainage densities, bedrock elevation, and relief (Beaumont et al., 2000; Bishop, 2007; Braun and Sambridge, 1997; Coulthard et al., 2000; Howard, 1994; Istanbuloglu and Bras, 2005; Paik, 2012; Tucker et al., 2001; Tucker and Hancock, 2010; Tucker and Slingerland, 1994; Willgoose et al., 1991). Thus LEMs offer the prospect of testing the fitness of various quantitative laws of diffusion (Martin and Church, 2004; Rempe and Dietrich, 2014; Roering et al., 1999; Tucker and Slingerland, 1994), advection

(Howard, 1994; Tucker and Bras, 1998; Tucker and Slingerland, 1994), and soil production processes (Heimsath et al., 1997, 2009; Roering, 2008). LEMs also allow us to generalize locally measured observations and fluxes to watershed and larger scales (Roering and Gerber, 2005; West et al., 2013), and reveal non-intuitive interactions between morphological processes and the resulting landforms (Perron et al., 2008, 2012; Willett et al., 2014).

The ever-growing interest in understanding the co-evolution of subsurface zone promotes the development of LEMs to consider more details of subsurface hydrological processes than heretofore included. This is needed, for example, in landscape-pedogenesis modeling which simulates soil evolution as a function of erosion and pedogenic processes because it shows a strong link between soil particle weathering and soil moisture (Cohen et al., 2010; Minasny et al., 2015). Also, Critical Zone (CZ) science, which studies the environmental gradient from atmosphere to bedrock at different spatial and temporal scales, sees surface and subsurface hydrological processes as vital at the air-soil and soil-bedrock interface (Anderson et al., 2008; Brantley et al., 2007). Moreover, where the infiltration capacity is high enough (Abrams et al., 2009; Higgins, 1982; Howard, 1988; Kochel et al., 1985; Laity and Malin, 1985; Lamb et al., 2008; Lobkovsky et al., 2007; Petroff et al., 2011, 2012, 2013; Schumm et al., 1995), the very nature of the landscape is different. Channels are formed by groundwater sapping such that the channels are bounded by steep walls and

* Corresponding author.

E-mail address: yzz130@psu.edu (Y. Zhang).

processes. Thus there is a need for a comprehensive, physically-based LEM that describes tectonics, bedrock evolution, and hill-slope and channel erosion by combining overland flow and groundwater seepage, and in which the groundwater is routed through the landscape subject to the co-evolution of surface topography, water infiltration, regolith thickness, and groundwater dynamics.

One key issue of conducting long-time scale modeling is to bridge the gap between short time-scale hydrodynamic processes and large time-scale morphodynamic processes. Ideally, we would simulate both sets of processes simultaneously, using short hydrological time steps to simulate millions of years of morphological change. However, this is not computationally possible at the present time, and an alternative acceleration approach must be found.

This paper aims to present a new, fully-coupled hydrologic-morphodynamic model that overcomes the limitations of earlier models to provide a platform for exploring the roles of rock uplift, weathering and incision, parameterized regolith creation by bedrock weathering and transport by advective and diffusive mechanisms (tree-throw and creep), fully coupled hydrologic processes of water infiltration (1-D), and lateral groundwater and surface water runoff (2-D) and evapotranspiration. We first provide the model design and theoretical development, and then conduct a series of numerical experiments to demonstrate the capabilities of the model. To overcome the difficulties of simultaneously solving a set of ordinary differential equations containing slow and fast processes, we present a morphological acceleration strategy. Some guidance is provided on choosing an optimal scaling factor, and model sensitivity to mesh geometry is explored.

2. Methodology

This section describes the design of the architecture of the multiscale hydrologic-morphodynamic model, the governing equations, the numerical method, the morphological acceleration strategy, and input data.

2.1. System design

The landscape evolution model presented here (LE-PIHM) is built on the Penn State Integrated Hydrologic Model (PIHM)—a multi-process, multi-scale hydrologic model where the major hydrological processes are fully coupled using the semi-discrete finite volume method (Qu and Duffy, 2007). LE-PIHM tracks seven state variables as functions of position and time: 1) the canopy water storage, 2) snow, 3) the surface water depth, 4) water storage in the unsaturated zone, 5) elevation of the groundwater table, 6) ground surface elevation, and 7) bedrock surface elevation. Fig. 1 describes the workflow of LE-PIHM. In this figure, PIHMgis, an open source GIS tool for data pre-process, decomposes a research domain into TINs (Triangular Irregular Network), prepares input files from raw data, and sets up the initial and boundary conditions of the research domain (for details of PIHMgis refer to Bhatt et al., 2014). In each simulation time step, LE-PIHM simulates landscape evolution by tightly coupling hydrological processes in the hydrological module and morphological processes in the morphological module, where these processes are represented by a mixture of physically-based ordinary differential equations (ODEs) and partial differential equations (PDEs). The governing equations of hydrological processes include ODEs for canopy interception, snowmelt, and evapotranspiration, and PDEs for infiltration, recharge, groundwater flow, and surface water flow. The morphological processes are governed by the PDEs describing bedrock uplift, regolith production and its downslope movement by tree-throw and creep, and sediment transport by streams. The numerical method of forming

global ODEs from local ODEs is introduced in subsection 2.5.

2.2. The morphological processes of LE-PIHM

The hydrological and morphological modules are fully-coupled in a two-layer system of regolith and impermeable bedrock (Fig. 2). The morphological state variables to be computed as functions of horizontal position (x, y), and time (t) are the ground surface elevation z (m), and the bedrock surface elevation e (m).

Applying the conservation of mass for regolith and bedrock within a control volume ($dx \times dy \times z$), the time rate of change of mass of regolith and bedrock yields:

$$\begin{aligned} \frac{\partial(\sigma_{re}h dx dy)}{\partial t} + \frac{\partial(\sigma_{ro}e dx dy)}{\partial t} &= \sigma_{re}q_c dy - \left[\sigma_{re}q_c dy + \frac{\partial(\sigma_{re}q_c dy)}{\partial x} dx \right] \\ &+ \sigma_{re}q_c dx - \left[\sigma_{re}q_c dx + \frac{\partial(\sigma_{re}q_c dx)}{\partial y} dy \right] \\ &+ \sigma_{re}q_s dy - \left[\sigma_{re}q_s dy + \frac{\partial(\sigma_{re}q_s dy)}{\partial x} dx \right] \\ &+ \sigma_{re}q_s dx - \left[\sigma_{re}q_s dx + \frac{\partial(\sigma_{re}q_s dx)}{\partial y} dy \right] \\ &+ \sigma_{ro}U dx dy \end{aligned} \quad (1)$$

where h, e, U, q_c and q_s are defined in Fig. 2. σ_{ro} and σ_{re} are the bulk densities of bedrock and regolith (kg/m^3), respectively. The time rate of change of mass of bedrock equals

$$\frac{\partial(\sigma_{ro}e dx dy)}{\partial t} = -\sigma_{ro}B_w dx dy + \sigma_{ro}U dx dy \quad (2)$$

where B_w is the rate of conversion of bedrock to regolith by bedrock weathering (m/yr). By definition, the thickness of regolith is the difference between ground surface elevation and bedrock elevation.

$$\frac{\partial h}{\partial t} = \frac{\partial(z - e)}{\partial t} \quad (3)$$

Cancelling terms and substituting equations (2) and (3) into (1), yields

$$\frac{\partial z}{\partial t} = \left(\frac{\sigma_{ro}}{\sigma_{re}} - 1 \right) B_w - \nabla \cdot q_c - \nabla \cdot q_s + U \quad (4)$$

and

$$\frac{\partial e}{\partial t} = -B_w + U \quad (5)$$

where ∇ is defined as $\nabla = \hat{x} \frac{\partial}{\partial x} + \hat{y} \frac{\partial}{\partial y}$ and \hat{x} and \hat{y} are unit vectors in x and y directions, respectively.

The left hand side (LHS) of equation (4) is the time rate of change of ground surface with respect to a fixed datum. The first term on the right hand side (RHS) of equation (4) is the change of ground surface elevation due to the volumetric expansion of regolith due to bedrock weathering (an external forcing variable). The second term represents the elevation change due to the net lateral volumetric regolith flux, and the third term is the elevation change due to the net surface flux by overland and channelized flow. The fourth term represents the elevation change due to bedrock uplift. The LHS of equation (5) represents the time rate of change of bedrock elevation with respect to the datum. The first term on the RHS represents the rate of bedrock loss by conversion to regolith and the second term

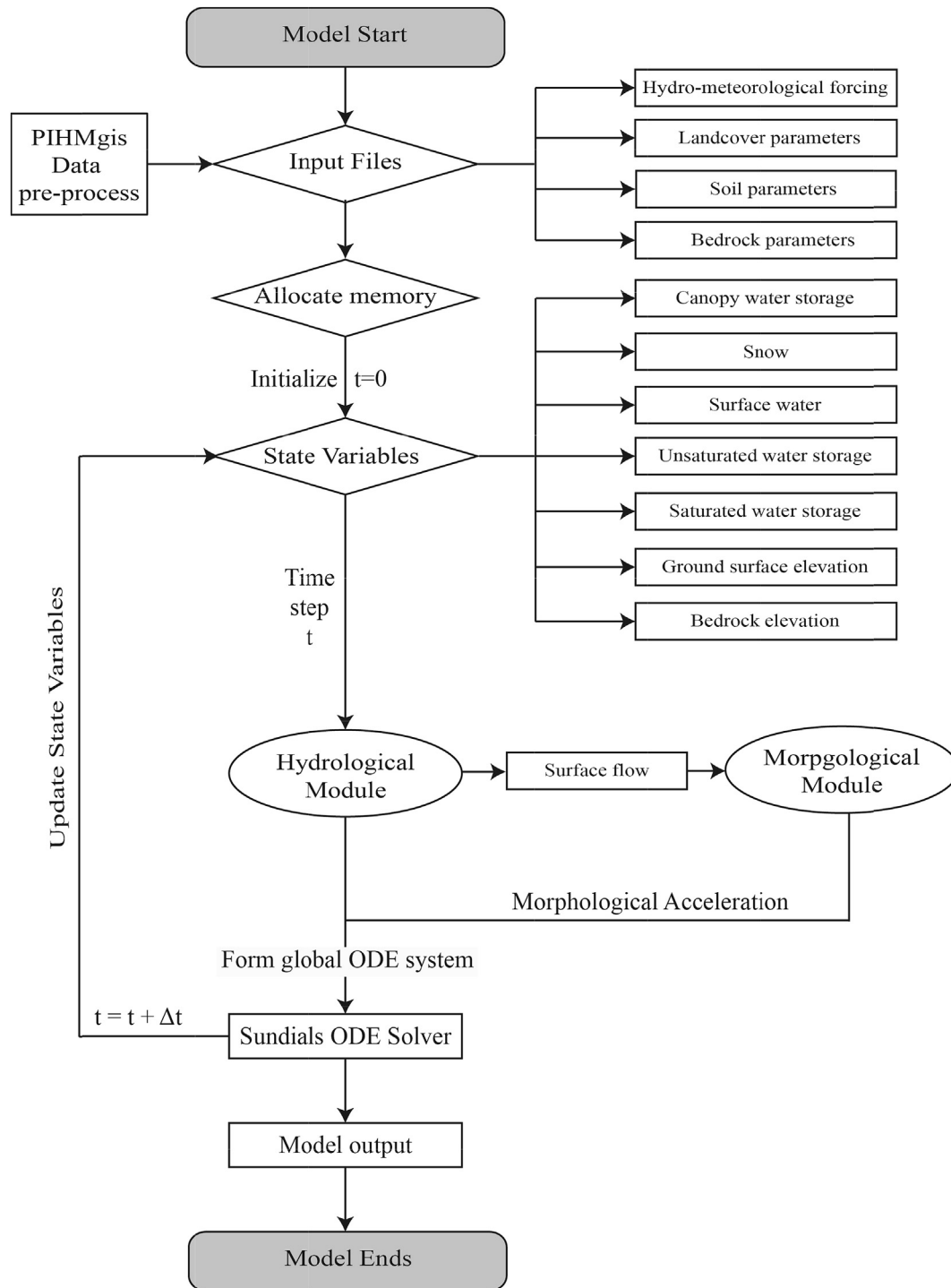


Fig. 1. Workflow diagram of LE-PIHM.

represents the elevation change of the bedrock due to tectonic uplift.

2.2.1. Regolith production by bedrock weathering

Weathering in the model is defined as the conversion of bedrock to regolith. The rate of conversion, B_w , was thought by Gilbert and Dutton (1880) to be a function of the depth of soil. Subsequent studies (e.g., Ahnert, 1977; Dietrich et al., 2003; Dietrich and Perron, 2006; Heimsath et al., 1997; Tucker and Hancock, 2010) have

quantified this dependency parametrically as (Heimsath et al., 2000):

$$B_w(x, y) = P_0 \exp[-\alpha H(x, y)] \sec \theta \quad (6)$$

where P_0 is the potential (or maximum) weathering rate of bare bedrock (m yr^{-1}), α is an empirical constant (m^{-1}), in one study equal to 0.022 (Heimsath et al., 1997), $H(x, y)$ equals the normal-slope regolith thickness at location x and y (m), and θ is the angle of slope in radians. However, *in-situ* measurements of soil

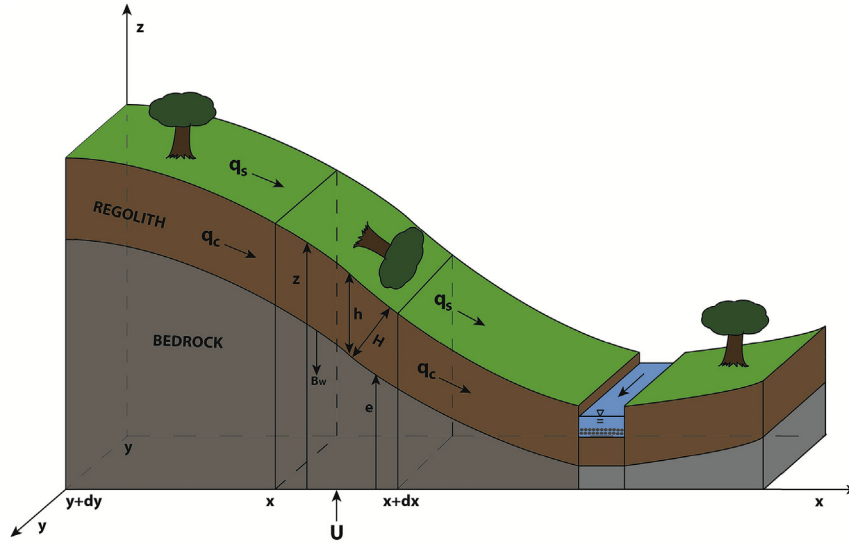


Fig. 2. Definition sketch of 3-D control volume on hillslope, where $z(x, y, t)$ = ground surface elevation (m), $e(x, y, t)$ = bedrock-regolith interface elevation (m), $h(x, y, t)$ = regolith thickness in vertical (m) (slope-normal thickness, H , is equal to $h \cos \theta$, where θ is the landscape surface slope), $U(x, y, t)$ = rock uplift rate (m yr^{-1}), $B_w(x, y, t)$ = bedrock weathering rate (m yr^{-1}) in the vertical direction, q_s = the surface flux of regolith sediment by overland flow ($\text{m}^2 \text{yr}^{-1}$), and q_c = the lateral volumetric regolith flux by creep and tree throw ($\text{m}^2 \text{yr}^{-1}$) entering through the sides of the control volume. The bottom of the stream may consist of alluvial deposits on bedrock.

production rate (e.g., Heimsath et al., 2001, 2009; Small et al., 1999) provide evidence of a humped relationship between soil production rate and thickness of overlying regolith. These observations support the initial intuition of Gilbert (1877) that the soil production rate may be maximized at some critical (nonzero) soil thickness, below which the weathering rate is reduced due to a lack of water for decomposing bedrock. Consequently, Anderson (2002) introduced a “humped” function, representing a combination of physical and chemical weathering:

$$B_w = \min\left(A_0 + bh, A_1 e^{-\frac{h}{h^*}}\right) \quad (7)$$

where the weathering rate, B_w , takes the minimum of the two terms in the parentheses. $A_0 + bh$ represents a linear relationship between weathering and thickness of regolith from the ground surface to the “critical depth”, h^* , where A_0 is the rate for bare bedrock; b is the weathering rate constant; A_1 is the maximum rate at the depth of h^* . Equation (7) introduces additional parameters that are not easily obtained from limited measurements. For the present we use equation (6), which agrees well with measurements in soil-mantled areas (Heimsath et al., 2000, 1997, 2009).

2.2.2. Lateral volumetric regolith flux

The second term on the RHS of equation (4) represents all regolith lateral movement through the control volume sides arising from gravity-driven processes, such as downslope fluxes associated with expansion and contraction due to moisture changes or freezing-thawing action (Anderson, 2002; Davison, 1889; Kirkby, 1967), ravel (Gabet, 2003; Roering and Gerber, 2005), transport by animals (e.g., gophers) (Gabet, 2000), and tree-throw (Gabet and Mudd, 2010; Norman et al., 1995). Here we lump these processes into two classes: creep (Sharp, 1982; Tucker and Hancock, 2010) and tree-throw (Roering et al., 2010).

The estimation of downslope flux by creep is based on the hypothesis that the average mass movement on a hillslope takes place at a rate proportional to the surface gradient (e.g. a diffusive process). As an example, upon freezing, regolith moisture expands. Assuming isotropic expansion, the regolith particles will move towards the ground surface and perpendicular to it (Kirkby, 1967).

When the frozen soil melts, the particles will fall vertically, having been displaced a horizontal distance proportional to the initial displacement distance, d , and the surface slope, $\tan(\theta)$. Thus, the downslope flux for one freeze-thaw cycle is proportional to $d \tan(\theta)$. If toppling is involved, as for example with surface ice needles (Matsuoka, 1998), then the flux is proportional to $\tan^2(\theta)$. Given the general acceptance of a linear dependency on slope (e.g., Culling, 1963; Martin and Church, 2004; Scheidegger, 1961; Tucker and Hancock, 2010) we take the lateral volumetric regolith flux by creep, q_{c1} , as:

$$q_{c1} = -K_1 \nabla z \quad (8)$$

where K_1 is the diffusivity ($\text{m}^2 \text{yr}^{-1}$), dependent upon the particular processes. But we note that for regolith-mantled slopes steeper than a critical threshold, the linear diffusion equation is insufficient to reflect the relationship between creep and slope angle (Andrews and Bucknam, 1987; Furbish et al., 2009; Gabet, 2000; Martin and Church, 1997; Roering, 2008; Roering et al., 1999, 2001). For these steeper slopes, a nonlinear flux law use the form (Roering, 2008):

$$q_{c1} = -\frac{K_2 \nabla z}{1 - (|\nabla z|/S_c)^2} \quad (9)$$

where S_c is the critical gradient at which flux becomes infinite and K_2 is a transport coefficient ($\text{m}^2 \text{yr}^{-1}$). The examples presented below use equation (8).

Although research on tree throw has been conducted for more than a century (Armson and Fessenden, 1973; Baker, 1915; Gabet and Mudd, 2010; Gabet et al., 2003; Hellmer et al., 2015; Norman et al., 1995; Ruel, 2000; Schaetzl et al., 1989; Ulanova, 2000), it was Gabet et al. (2003) who first derived an equation predicting the resulting regolith flux. They assumed that trees topple over by a simple hinge fall where the axis of rotation is at the downhill edge of the pit and the root plate comes to rest at approximately right angles to the regolith surface. The volumetric horizontal flux of regolith in the downslope direction per unit width due to tree throw, q_{c2} , is given by (Gabet et al., 2003):

$$q_{c2} = c_1 * c_2 * c_3 * c_4 \quad (10)$$

where c_1 represents volume of tree root plat per tree throw event ($m^3/event$), which varies as a function of tree species and regolith thickness; the second term on the RHS of equation (10) is the net downslope distance per event, c_2 , derived by Gabet et al. (2003) as:

$$c_2 = \frac{2}{\pi} (W + D) \sin \theta \quad (11)$$

where W is the width of the root plate, D is the pit depth, and θ is the slope angle. Data from a deciduous forest in northern Michigan suggest that $W = 4$ m and $D = 0.7$ m (Norman et al., 1995). The third and fourth terms on the RHS of equation (10) represent the density of tree throw event ($event/m^2$) and the frequency of tree throw event ($event/yr$), respectively. These parameters can be derived from in-situ measurement. Thus equation (10) takes the form:

$$q_{c2} = -K_3 \sin \theta \quad (12)$$

where $K_3 = 4.8 \times 10^{-3} (m^2 yr^{-1})$ (Gabet et al., 2003). If the slope is shallow ($\theta < 5^\circ$), we may approximate $\sin \theta \approx \tan \theta = \nabla z$, and thereby $q_{c2} = -4.8 \times 10^{-3} \nabla z$. The parameter K_3 varies as a function of different tree species.

2.2.3. Sediment flux by overland and channelized flow

The dimensionless surface sediment flux, q_s^* , accounts for all regolith material transported into and out of the control volume by running water. A common and useful approach is to empirically relate it to either the dimensionless Shields stress τ^* or the excess of the Shields stress above some appropriately defined critical Shields stress τ_c^* . Prosser and Rustomji (2000) reviewed the approaches of estimating sediment transport by overland flow, as for example from Wong and Parker (2006) for bedload:

$$q_s^* = 3.97 (\tau^* - \tau_c^*)^{3/2} \quad (13)$$

where q_s^* is also called the dimensionless Einstein number. The bedload sediment flux, q_s , is expressed as a dimensionless Einstein number:

$$q_s^* = \frac{q_s}{\sqrt{Rg} D_{50} D_{50}} \quad (14)$$

where $R = \frac{\rho_s}{\rho} - 1$ = submerged specific gravity of sediment; ρ is fluid density; ρ_s is the density of sediment (kg/m^3); g is gravity; and D_{50} is the median diameter of sediment particles (m). The Shields stress τ^* in equation (13) is defined as:

$$\tau^* = \frac{\tau_0}{(\rho_s - \rho)gD_{50}} \quad (15)$$

where τ_0 is the shear stress ($kg m^{-1} s^{-2}$). In the model, τ_0 is calculated from the quadratic shear stress law:

$$\tau_0 = \rho C_f V^2 \quad (16)$$

where C_f is the drag coefficient (dimensionless) and V is the vertical average velocity of overland flow ($m s^{-1}$) and calculated by equation (25). Note that the unit of flow velocity for hydrological simulation is m/day . Here, we convert the unit to m/s and calculate bedload sediment transport rate, and then the unit of the bedload sediment transport rate is converted to m^2/yr .

Definition of the critical Shields stress follows Parker et al. (2003) for fully rough flow in gravel-bed rivers:

$$\left\{ \begin{array}{l} \tau_c^* = 0.5 \times \left[0.22 \times R_{eD}^{-0.6} + 0.06 \times \exp(-17.77 R_{eD}^{-0.6}) \right], 0 < R_{eD} < 60 \\ 0.045, R_{eD} > 60 \end{array} \right. \quad (17)$$

where R_{eD} is the particle Reynolds number defined as:

$$R_{eD} = \frac{u_* D_{50}}{\nu} \quad (18)$$

and D_{50} is the median diameter of the sediment particles (m), ν is the kinematic viscosity (m^2/s^2), and u_* is the fluid shear velocity (m/s) equal to:

$$u_* = \sqrt{\frac{\tau_0}{\rho}} \quad (19)$$

2.2.4. Rock uplift

The fourth term on the RHS of equation (4) represents the mass entering the control volume by rock uplift. The word “uplift” refers to displacement of rock in the direction opposite to the gravity vector. Although the uplift rate is a function of location (x, y), in the examples presented here the uplift rate is spatially invariant and set to the magnitude of rock uplift rates in the Middle Atlantic States of the US during the Cenozoic. These range between $5m/Myr - 30m/Myr$ above knickpoints and $50m/Myr - 100 m/Myr$ below knickpoints (Miller et al., 2013).

2.3. The hydrological processes of LE-PIHM

The hydrological processes track the time rate of change of water storage from vegetation canopy to soil zone. The governing equations for the hydrological processes follow PIHM (Kumar, 2009; Qu and Duffy, 2007):

$$\left\{ \begin{array}{l} \frac{\partial \Psi_{canopy}}{\partial t} = vFrac * (1 - f_s) * P - E_c - TF \\ \frac{\partial \Psi_{snow}}{\partial t} = f_s * P - SM \\ \frac{\partial \Psi_{surf}}{\partial t} = \nabla q_{sw} + P_{net} - I - E_s \\ \frac{\partial \Psi_{unsat}}{\partial t} = I - R - E_g - E_{gt} \\ \frac{\partial \Psi_{sat}}{\partial t} = \nabla q_{gw} - R - E_{sat} - E_{tsat} \end{array} \right. \quad (20)$$

where Ψ_{canopy} , Ψ_{snow} , Ψ_{surf} , Ψ_{unsat} and Ψ_{sat} are canopy water storage (m), snow (m), the surface water depth (m), water storage in the unsaturated zone (m), water storage in the saturated zone (m), respectively. $vFrac$ is the fraction of vegetation coverage; f_s is the fraction of snow; P is the precipitation rate (m/day); E_c is the evaporation on canopy (m/day); TF is the water through fall (m/day); SM is the snow melt (m/day); P_{net} is the water reaching ground surface (m/day); I is the infiltration rate (m/day) predicted by

$$I = K(\Psi) \frac{(\Psi_{surf} + z) - (\Psi + e)}{d} \quad (21)$$

where Ψ is the water head of unsaturated water or saturated water. It depends on the level of saturation. If soil zone becomes saturated, $\Psi = \Psi_{sat}$. Otherwise, $\Psi = \Psi_{unsat}$. d is the distance between the centroid of surface water and unsaturated zone or saturated zone

(m), $K(\Psi)$ is calculated by using Van Genuchten equation (Van Genuchten, 1980); E_s , E_g and E_{sat} are evaporation (m/day) from surface water, unsaturated water and saturated water, respectively. These evaporation rates are estimated by using the Penman equation (Bras, 1990):

$$E_s = (1 - vFrac) \frac{\Delta(R_n - G) + \rho_a C_p (\varepsilon_s - \varepsilon_a)}{\Delta + \gamma} \quad (22)$$

$$E_g \text{ or } E_{sat} = \beta_s E_s \quad (23)$$

$$\beta_s = \begin{cases} 0.5 \left(1 - \cos \left(\pi \frac{\theta_g}{\theta_{fl}} \right) \right) & \theta_g \leq \theta_{fl} \\ 1 & \theta_g > \theta_{fl} \end{cases} \quad (24)$$

where R_n is the net radiation (W/m^2); G is soil heat flux (W/m^2); ρ_a is the air density (kg/m^3); C_p is specific heat of the air; $\varepsilon_s - \varepsilon_a$ represents the air vapor pressure deficit; Δ is slope of the saturation vapor pressure-temperature relationship; γ is the psychrometric constant; β_s describes the influence of the top soil layer saturation on evaporation from ground; $\theta_{fl} = 0.75\theta_{sat}$ is the field capacity; θ_{sat} is saturated soil moisture content; θ_g is the soil moisture content of the top soil layer, which is related to Ψ_{unsat} ; R is the recharge rate (m/day); E_{gt} and E_{tsat} are the transpiration rate (m/day) from unsaturated zone and saturated zone, respectively; q_{sw} represents the volumetric overland flow per unit width (m^2/day) predicted by the diffusion wave approximation of St. Venant's equation assuming shallow water depth and negligible influence of inertia force (Gottardi and Venutelli, 1993), which is equivalent to Manning's equation. By defining the terms of conductivity and gradient of surface water head, the equation for overland flow yields

$$V = \Gamma_{surf} * grad \Psi_{surf} \quad (25)$$

$$q_{sw} = V * \Psi_{surf} \quad (26)$$

$$\Gamma_{surf} = \frac{\Psi_{surf}^{2/3}}{n_s} \left(\nabla \cdot (\Psi_{surf} + z) \right)^{-1/2} \quad (27)$$

$$grad \Psi_{surf} = \nabla \cdot (\Psi_{surf} + z) \quad (28)$$

where Γ_{surf} is the conductivity; $grad \Psi_{surf}$ represents the gradient of surface water head; n_s is the Gauckler–Manning coefficient ($day/m^{1/3}$). q_{gw} is the volumetric lateral groundwater flow per unit width

(m^2/day) predicted by

$$q_{gw} = \Psi_{sat} \Gamma_{sat} grad \Psi_{sat} = \Psi_{sat} \Gamma_{sat} \nabla \cdot (\Psi_{sat} + e) \quad (29)$$

where Γ_{sat} is the horizontal hydraulic conductivity (m^2/day).

The surface elevation, z , and bedrock elevation, e , are coupled in equations (27)–(29), respectively, meaning that the gradient of hydraulic head varies with the real-time change of both the hydrological and morphological state variable. In this study, we neglect vegetation interception and transpiration, and snow.

One important feature of the model is the consideration of the effect of macropores on subsurface flow. Macropores such as root holes, cracks or pipes in soils, or fractured bedrock can result in preferential flow, like large and fast infiltration, recharge, and lateral groundwater flow (Aubertin, 1971; Beven and Germann, 1982, 2013; Bouma, 1981; Faeh et al., 1997; Thomas and Phillips, 1979; Weiler and Naef, 2003). Even though the fraction of macropores is small relative to the soil matrix, the volumetric transport capacity can be significant to the overall flow. We defined the soil zone as a dual matrix-macropore system where the macropore effect is taken into account to calculate the effective hydraulic conductivity for infiltration lateral subsurface flow. The effective hydraulic conductivity, K_{eff} , is defined as a weight function of matrix conductivity, K_{mat} , and macropore conductivity, K_{mac} .

$$K_{eff}(\Psi) = K_{mat}(\Psi) * (1 - mFrac) + K_{mac}(\Psi) * mFrac * [S] \quad (30)$$

where $mFrac$ is the fraction of macropore in soil zone, $[S]$ is the level of soil saturation. $K_{mat}(\Psi)$ and $K_{mac}(\Psi)$ are calculated by using Van Genuchten equation (Van Genuchten, 1980). Equation (30) indicates that the macropore effect increase with level of soil saturation. LE-PIHM provides options of turning on or off the macropore effect. More details about each term of the governing equations can be found in (Kumar, 2009; Qu and Duffy, 2007).

2.4. Domain decomposition

The set of equations solved in LE-PIHM for the 7 state variables are summarized in Table 1. Solutions are obtained using the finite volume method. First, the geographic region of interest is decomposed into an unstructured triangular mesh. LE-PIHM uses Delaunay Triangulation to generate unstructured triangular meshes that meet the common shape criterion of Teng and Wong (2000), such that the angles of each element are neither too small nor too large. It should be noted that this approach differs from PIHM (Qu and Duffy, 2007) which divides the domain into two parts—a triangular mesh on hillslopes and a rectangular mesh simulating river channels. The

Table 1

Governing equations on a model control volume with corresponding ODEs that define the model kernel. See the definition of all symbols in **nomenclature**.

Description	Original governing equations	Semi-discrete form ODEs
Surface elevation	$\frac{\partial z}{\partial t} = \left(\frac{\sigma_{ro}}{\sigma_{re}} - 1 \right) B_w$ $-\nabla \cdot q_c - \nabla \cdot q_s + U$	$\frac{dz}{dt} = \left(\frac{\sigma_{ro}}{\sigma_{re}} - 1 \right) B_w - \sum_j \frac{Q_{w,j}}{A_i} - \sum_j \frac{Q_{w,j}}{A_i} + U_i$
Bedrock elevation	$\frac{de}{dt} = -B_w + U$	$\frac{de}{dt} = -B_w + U$
Vegetation canopy storage	$\frac{d\Psi_{canopy}}{dt} = vFrac * (1 - f_s) * P$ $-E_c - TF$	$\frac{d\Psi_{canopy}}{dt} = vFrac * (1 - f_s) * P - E_c - TF$
Snow	$\frac{d\Psi_{snow}}{dt} = f_s * P - SM$	$\frac{d\Psi_{snow}}{dt} = f_s * P - SM$
Surface water depth	$\frac{\partial \Psi_{surf}}{\partial t} = \nabla q_{sw} + P_{net} - I - E_s$	$\frac{d\Psi_{surf}}{dt} = \sum_{j=1}^3 \frac{Q_{w,j}}{A_i} + P_{net} - I - E_s$
Unsaturated water head	$\frac{d\Psi_{unsat}}{dt} = I - E_t - R - E_g - E_{gt}$	$\frac{d\Psi_{unsat}}{dt} = I - E_t - R - E_g - E_{gt}$
Groundwater head	$\frac{\partial \Psi_{sat}}{\partial t} = \nabla q_{gw} + R - E_{sat} - E_{tsat}$	$\frac{d\Psi_{sat}}{dt} = \sum_{j=1}^3 \frac{Q_{w,j}}{A_i} + R - E_{sat} - E_{tsat}$

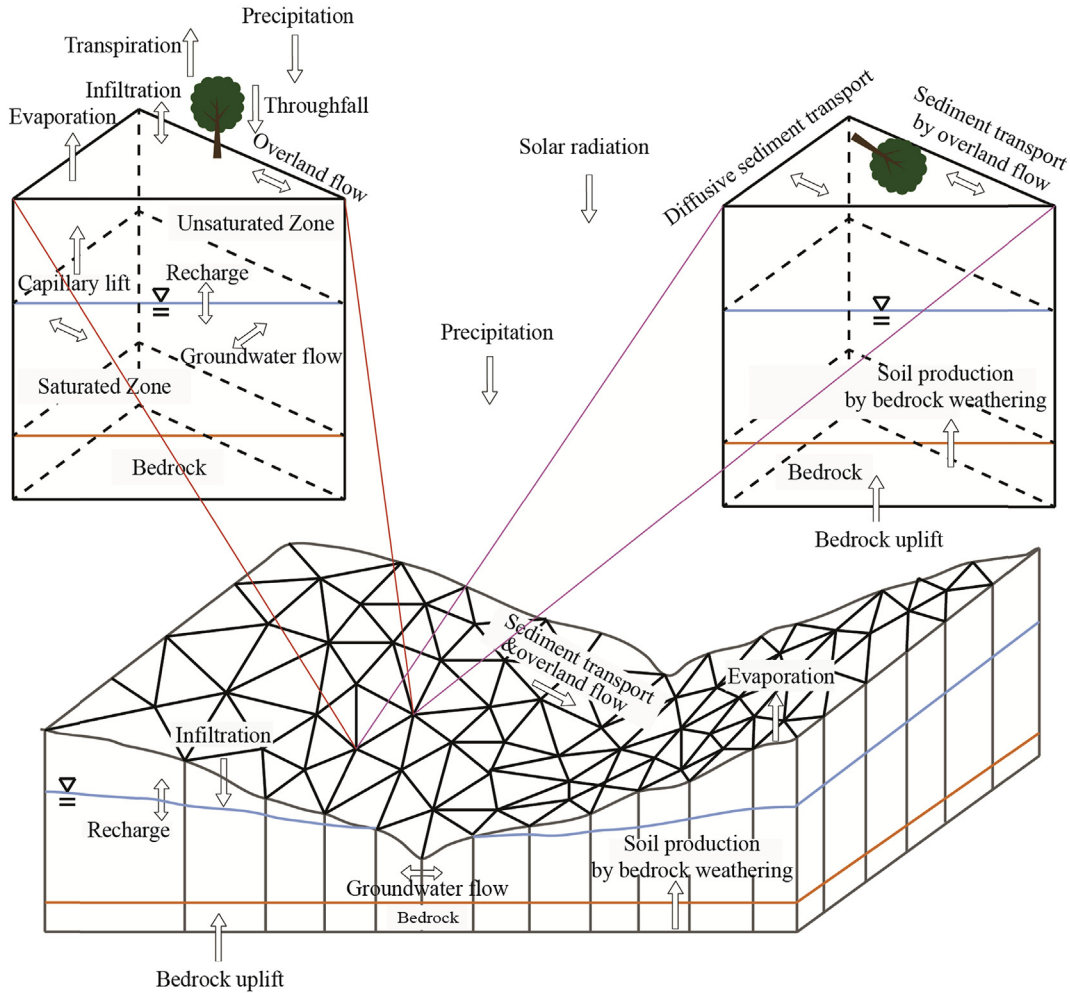


Fig. 3. 3-D sketch of the components of processes in control volumes and model domain of LE-PIHM (modified from Bhatt et al., 2014). The top left prism is an example of processes in the hydrological module (see the module in Fig. 1). The top right prism, which actually is the same one as the left prism, illustrates processes in the morphological module (see the module in Fig. 1). The model forms a local ODE system for each of the prisms and assembles these local ODE systems into a global ODE system for the whole model domain shown in the bottom.

PIHM approach is not possible for landscape evolution studies where the locations of the streams are not known *a priori*. Therefore, LE-PIHM decomposes the model domain into only a triangular mesh (see the decomposed model domain in Fig. 3).

2.5. Numerical method

To obtain solutions the semi-discrete finite volume method is applied to the governing equations, thereby converting them to ordinary differential equations in time (Table 1). Given N computation cells, then N local systems of ODEs are assembled to form a global ODE system. The global system is then solved by an ODE implicit solver to advance the solution one time step.

The original system of equations is locally reduced to ordinary differential equations (ODEs) by integration on a spatial unit element. Partial differential equations are integrated over three dimensional control volume, V_i , in the model domain as, for example for equations (4) and (5):

$$\int_{V_i} \frac{\partial z}{\partial t} dV = \int_{V_i} \left(\frac{\sigma_{ro}}{\sigma_{re}} - 1 \right) B_w dV - \int_{V_i} \nabla q_c dV - \int_{V_i} \nabla q_s dV + \int_{V_i} U dV \quad (31)$$

$$\int_{V_i} \frac{de}{dt} dV = - \int_{V_i} B_w dV + \int_{V_i} U dV \quad (32)$$

By applying Gauss's theorem on equations (26) and (27), we obtain

$$\frac{\partial}{\partial t} \int_{V_i} z dV = \int_{V_i} \left(\frac{\sigma_{ro}}{\sigma_{re}} - 1 \right) B_w dV - \int_{A_{ij}} \vec{n} \cdot q_c dA - \int_{A_{ij}} \vec{n} \cdot q_s dA + \int_{V_i} U dV \quad (33)$$

$$\frac{d}{dt} \int_{V_i} e dV = - \int_{V_i} B_w dV + \int_{V_i} U dV \quad (34)$$

where \vec{n} is the normal vector to the surface j of the control volume V_i . By integrating the individual terms in equations (28) and (29), we obtain a semi-discrete form of ODE that defines all of the morphological processes incorporated in the finite volume of the model:

$$\frac{dz}{dt} = \left(\frac{\sigma_{ro}}{\sigma_{re}} - 1 \right) B_w - \sum_j \frac{Q_{c,ij}}{A_i} - \sum_j \frac{Q_{s,ij}}{A_i} + U_i \quad (35)$$

$$\frac{de}{dt} = -B_w + U \quad (36)$$

where $Q_{c,ij}$ and $Q_{s,ij}$ are the volumetric sediment flux by creep and tree-throw, and overland flow, respectively. $Q_{c,ij}$ equals the product of q_c times the width of the i th control volume in the j th direction. $Q_{s,ij}$ equals the product of q_s and the width of the i th control volume in the j th direction. The same finite volume strategy has been used on the PDEs for the hydrological processes. See all the semi-discrete forms of the ODEs in Table 1.

The global ODE system representing both morphological processes and hydrological processes is solved simultaneously using the Newton-Krylov implicit ODE solver CVODE (Cohen and Hindmarsh, 1996). The solver is a typical choice for large non-linear stiff ODE system (Jones and Woodward, 2001). CVODE uses a combination of the Backward Difference Formula (BDF) with linear Krylov iteration, and a preconditioned GMRES algorithm (Byrne, 1992).

2.6. Morphological acceleration: a computational necessity

A system of ODEs representing hydrological state variables that evolve over seconds to days and morphological state variables that evolve over days to millions of years presents a major computational challenge. To capture rainfall events requires a time step too small to feasibly compute landscapes that take millions of years to reach a steady-state under an average steady forcing. Two possible solutions are proposed. The first, Offline Updating, decouples the hydrodynamic and morphodynamic solutions by using time-averaged hydrological fluxes as a constant input for a certain time period of morphodynamic simulation, after which the hydrological solutions are updated using the new bedrock and topographic elevations. The limitation is that the hydrological processes can become decoupled from the topography resulting in non-unique landscapes dependent upon the duration between updates. The second method, Online Updating, overcomes this limitation by simultaneously computing the evolving hydrology and morphology using a morphological scaling factor. We use the latter approach.

The concept of a morphological scale factor was introduced by Lesser et al. (2004) and Roelvink (2006) for use in the morphodynamic modeling of coastal areas (George et al., 2012; Van der Wegen and Roelvink, 2008; Warner et al., 2008). Long morphological simulations can be achieved using hydrodynamic simulations of only a fraction of the required duration. For example, 100 years of meteorological forcing can be used to predict one million years of morphological change. In LE-PIHM one year or several years of hourly to daily meteorological forcing is repeated year after year. Morphological changes in the landscape during each time step are amplified by multiplying the erosional and depositional flux in a control volume at every hydrological time by a morphological scale factor (MSF). The equation can be expressed as

$$MSF = \frac{\text{Morphological time step}}{\text{Hydrological time step}} \text{ or } \Delta t_{morph} = MSF \Delta t_{hydro} \quad (37)$$

For instance, if $MSF = 100$ and $\Delta t_{hydro} = 1$ min, then $\Delta t_{morph} = 100$ min. Thus, morphological changes are accelerated by 100 times, which also means 1 min at a particular hydrological state produces 100 min of morphodynamic change. The concept is straightforward, but how to choose an appropriate MSF is complicated. The accuracy of MSF is discussed below.

2.7. Input data for LE-PIHM

We summarize the input data in Fig. 4. The name of the input file consists of a project name and an extension indicating the type of input data. For example, the “experiment1.soil” file indicates that the project name is experiment1, and the data type is soil data.

2.8. Experimental design

We present three synthetic experiments at different spatial scales to demonstrate the utility of LE-PIHM. The first experiment aims to explore the importance of coupling surface and ground-water processes. The goal of experiment 2 is to test the dependence of LE-PIHM on mesh structure. The last experiment discusses the criteria for finding an optimal MSF .

The first experiment is applied on a small model domain (2000 $m \times$ 2000 m), which is consistent with the model domain of a widely cited experiment in Tucker and Bras (1998). The second and the third experiments simulate landscape evolution at a larger spatial scale (15000 $m \times$ 15000 m). All experiments start from a flat land surface with uniform surface elevation (800 m) and bedrock elevation (790 m). Water and sediment are not allowed to pass through the boundaries except along the edges of the most southern element for experiment 1 and two adjacent elements on the central southern boundary for experiments 2 and 3. Initially, the groundwater table is set to 0.1 m below the ground surface, and there is no land surface water, unsaturated water, and water storage on the vegetation canopy. The parameters are summarized in Table 2.

3. Experiment 1: landscapes with and without groundwater flow

Experiment 1 includes two simulations: (1) landscape evolution with subsurface flow, and (2) landscape evolution without subsurface flow. The model domain has been decomposed into 2321 elements by using a maximum area of 2700 m^2 and a minimum angle of 33°. The averaged distance between two nodes is 40 m. For the simulation with subsurface flow, the groundwater table relaxes from a high level to its actual condition.

3.1. Comparison of landscape evolution with and without groundwater flow

In Fig. 5, the resulting landscape created by processes including subsurface flow has greater steady state relief (~20 m) and significantly different hillslope curvatures. Qualitatively, landscape (a) contains concave hillslopes, indicating that runoff erosion is the dominant hillslope process, because all precipitation must travel by overland flow. In contrast, the convex hillslopes in landscape (b) are the typical signature of a diffusion-dominant hillslope processes. This arises because at upland sites some of the precipitation travels to down-valley sites by traveling through the sub-surface.

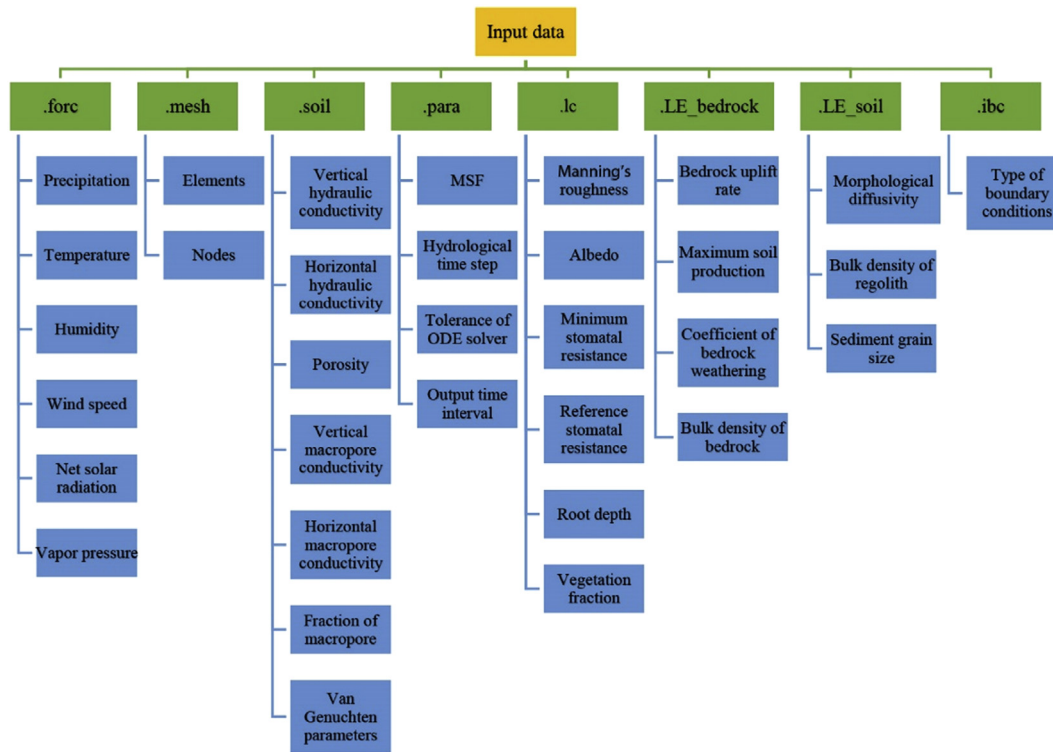


Fig. 4. Input files and parameters in each file for LE-PIHM.

Table 2
Parameters for experiment 1, 2 and 3.

Parameters	Description	Exp 1 with gw	Exp 1 w/o gw	Exp 2	Exp3
Δt_{hydro}	Hydrologic time step	1 min	1 min	1 min	1 min
MSF	Morphological scale factor	52,560	52,560	52,560	Multiple
P_0	Bare bedrock weathering rate (m/yr)	0.0004	0.0004	0.0004	0.0004
U	Bedrock uplift rate (m/yr)	0.0001	0.0001	0.0001	0.0001
D	Grain diameter (m)	0.0001	0.0001	0.0001	0.0001
K	Morphological diffusivity (m ² /year)	0.01	0.01	0.005	0.005
Prep	Precipitation	variable (annual 1.08 m)	variable (annual 1.08 m)	0.2 m/day	0.2 m/day
Γ_v	Vertical hydraulic conductivity	0.1 m/day	0.1 m/day	0.4 m/day	0.4 m/day
Γ_h	Horizontal hydraulic conductivity	10 m/day	10 m/day	10 m/day	10 m/day

Table 3
Computational time for each simulation.

Computational Environment: Processor: Intel Core i7 CPU 2.93GHz, Memory: 16GB
 Number of elements: 2321 (experiment 1), 1000 (averaged in experiment 2) and 924 (experiment 3)

MSF	Experiment 1	Experiment 2	Experiment 3
5256			
52,560	40 days	14 days	14 days
525,600			7 days
5,256,000			2 days

Slope-area relationships are a convenient method for quantifying these differences (Fig. 6) (McNamara et al., 2006). The steady state landscape with subsurface flow possesses steeper slopes for a given drainage area than the landscape without subsurface flow. These differences arise because overland flows are constrained by upslope infiltration and surface discharges that occur in the concave portion of the hillslopes near channels. Sediment transport rates are generally lower compared to the case that does not

include subsurface flow, and to balance rock uplift rates, slopes must increase to increase downslope diffusion processes. Fig. 6 shows a down-valley transition from diffusion-dominant erosive processes (positive S-A slope) to advective-dominant processes (negative S-A slope). However, the valley heads are located at different drainage areas for the two landscape types. The positive S-A slope occupies a very small portion of the S-A plot for the landscape without subsurface flow (solid black dots), therefore, the convex profile of hillslope occupies a small portion of the whole hillslope, which is consistent with the hillslope curvature shown in Fig. 5. Likewise, a larger portion of positive S-A slope for landscape with subsurface flow (black circle) indicates a larger portion of convex hillslope. After the turnover point, the power law relationship of slope and area for fluvial erosion becomes obvious.

These results can be compared to simulations in Tucker and Bras (1998) with the same key parameters, like the tectonic uplift rate, diffusivity, annual precipitation, and mesh geometry. Interestingly, our S-A plot shows a little steeper slope, which we attribute to the inclusion of processes such as bedrock weathering and soil production which are not considered in Tucker and Bras (1998).

The LE-PIHM simulated landscapes are qualitatively consistent

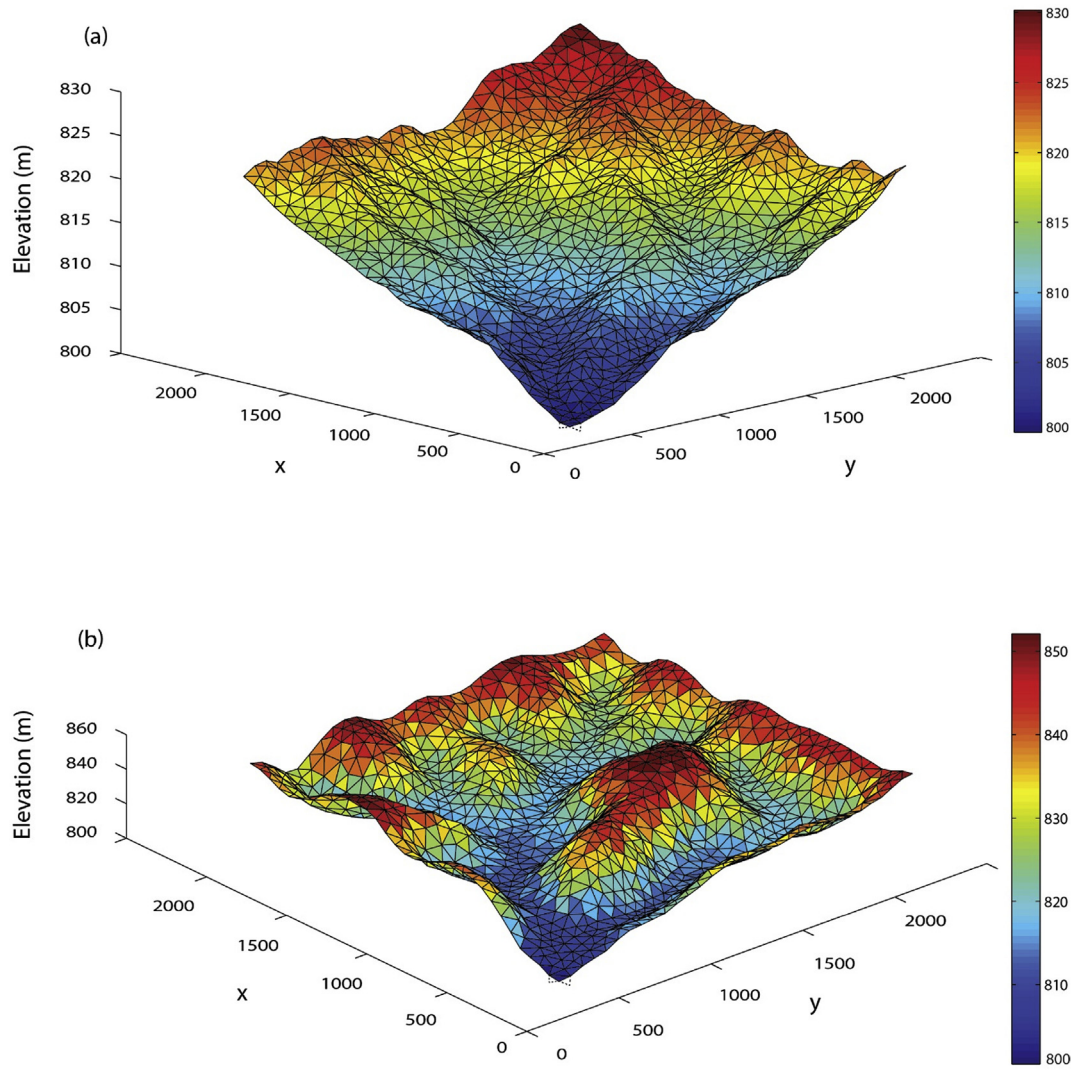


Fig. 5. Steady state landscapes without and with subsurface flow. Boundaries are no-flow boundaries, excepting the most southern element, in which water and sediment pass out of the mesh through the exterior face. (a) Steady state landscape without subsurface flow; (b) steady state landscape with subsurface flow. Color bar represents the elevation above sea level (m) coded from dark blue for low elevation to red for high elevation. See text for interpretation. (For interpretation of the references to color in this figure legend, the reader is referred to the web version of this article.)

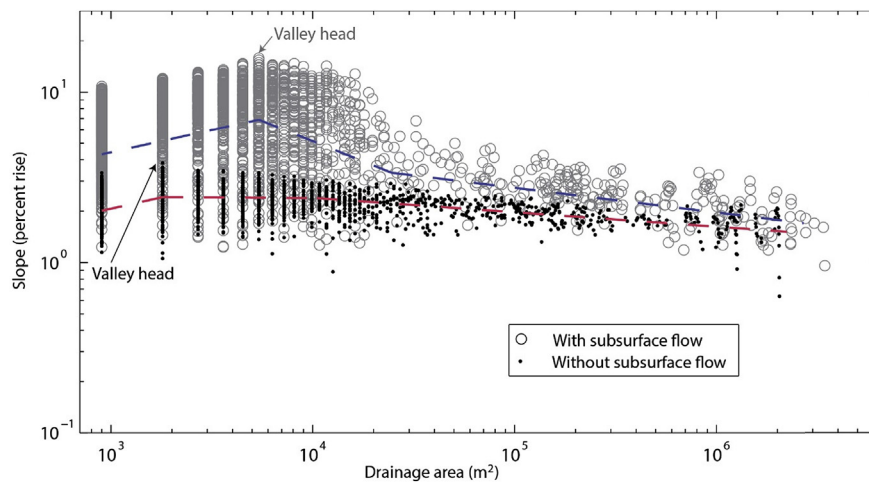


Fig. 6. Relationship between local slope and upslope drainage area for simulated steady state landscape with and without subsurface flow.

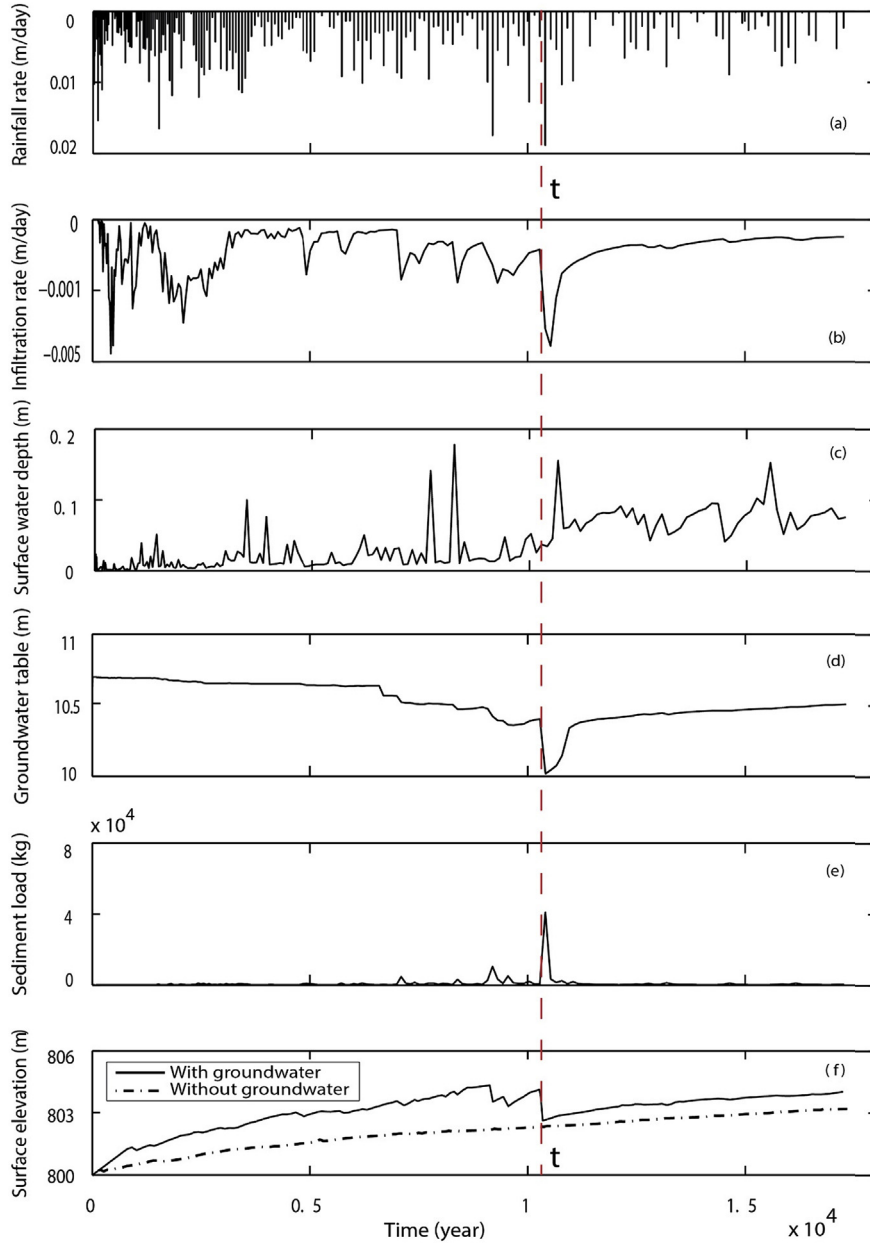


Fig. 7. The evolution of regolith moisture, infiltration, surface water depth, and surface elevation of the outlet (the most southern element of Fig. 5).

with field observations of stream- and groundwater-dominated landscapes, but are they quantitatively similar? To answer this question we examine the model output in light of the laws of drainage networks (Horton, 1945; Schumm, 1956):

$$N_i \cong \gamma_N^{\sigma-i} \quad (\text{Law of stream number}) \quad (38)$$

$$\bar{L}_i \cong \gamma_l^{\sigma-i} \quad (\text{Law of stream length}) \quad (39)$$

$$\bar{A}_i \cong \gamma_a^{\sigma-i} \quad (\text{Law of drainage area}) \quad (40)$$

where N_i is the number of streams of order i ; \bar{L}_i is the average length of streams of order i ; \bar{A}_i is the average drainage area of order i , and γ_N , γ_l and γ_a are bifurcation ratio, stream length ratio and drainage area ratio with observed ranges of $-1.6 \leq \log \gamma_N \leq -1$, $0.4 \leq \log \gamma_l \leq 1.25$ and $1 \leq \log \gamma_a \leq 1.8$, respectively. σ is the highest

order of the watershed domain. Let $b_1 = -\log \gamma_N$, $b_2 = \log \gamma_l$ and $b_3 = \log \gamma_a$. The ratio of b_1 over b_2 is defined as the fractal dimension, D_n . It reflects the space-filling of the river network, and lies near 2 (Braun and Sambridge, 1997; Rodriguez-Iturbe and Rinaldo, 2001; Tarboton et al., 1988).

The modeled landscapes produce channel networks for which $b_1 = 1.25$, $b_2 = 0.61$, and $b_3 = 1.33$ for landscape Fig. 5a, and $b_1 = 1.17$, $b_2 = 0.58$, and $b_3 = 1.20$ for landscape Fig. 5b. These fall within the range of drainage network observed in these settings. Furthermore, the fractal dimensions, $D_n = 2.04$ and $D_n = 2.01$ for landscape (a) and (b), are also similar to these observed drainage networks.

3.2. Hydrological and morphological interaction

Very few studies have modeled the impact of subsurface hydrology on landscape evolution in three dimensions (Barkwith

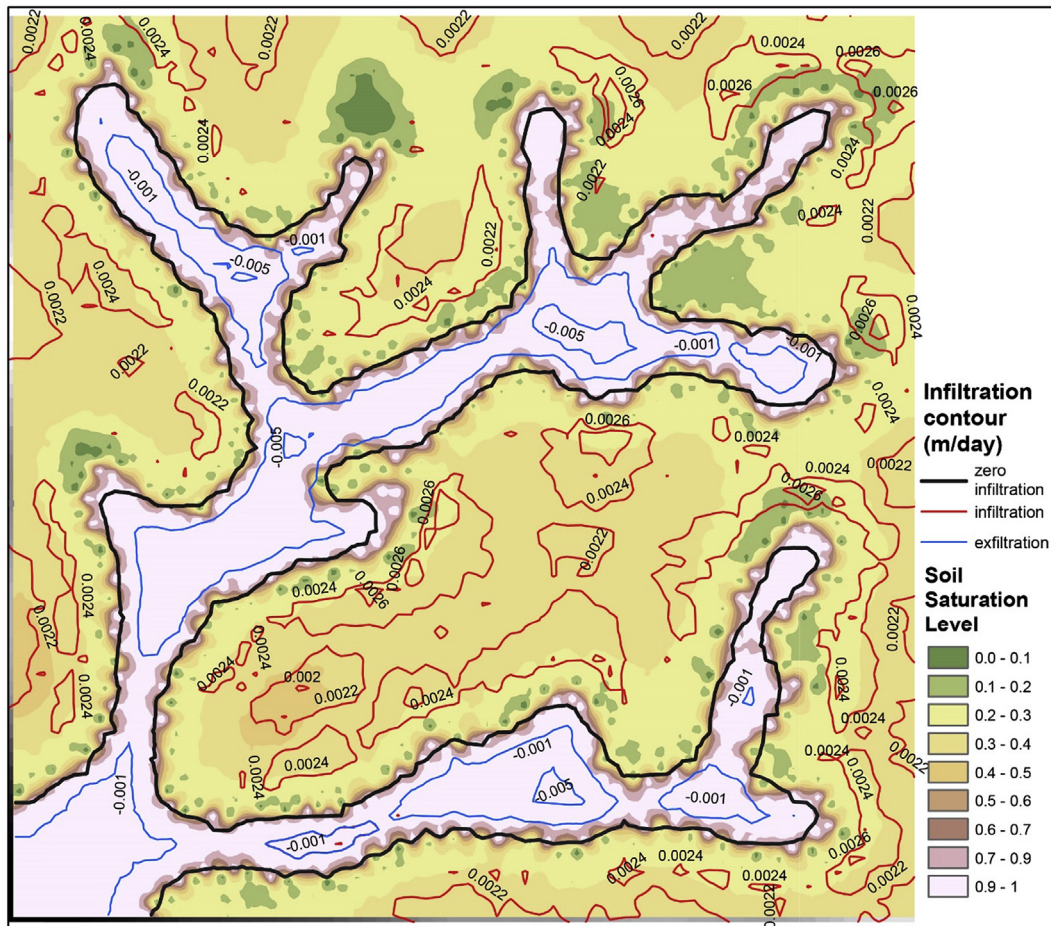


Fig. 8. Spatial distribution of infiltration and exfiltration (the rate in unit of meter per day).

et al., 2015; Francipane et al., 2012). Here, we isolate a computational element at the outlet in Expt. 1 with subsurface flow, and discuss the influence of hydrological processes on the sediment transport and landscape erosion of the catchment (Fig. 7). At the beginning of the simulation, groundwater flows to the outlet due to the elevation gradient caused by bedrock uplift. Groundwater converges to this element making the groundwater head greater than surface water head, thereby groundwater seepage occurs (negative infiltration in Fig. 7b). At this time, the variation of infiltration mainly results from the initial condition. Afterwards, the influence of the initial condition decreases, and the groundwater table elevation becomes adjusted to meteorological forcing. Meanwhile, there is no sediment transport by overland flow because the shear stress of overland flow doesn't exceed the critical shear stress (Fig. 7e). Later on, sediment transport occurs because large rainfall events raise surface water depth and accelerate the infiltration rate.

By time t , a spike of infiltration is stimulated by several contiguous rain storms, thereby increasing groundwater exfiltration, surface water depth, and surface water gradient (Fig. 7c). With an increase in surface water gradient, sediment load increases rapidly, and the increased sediment flux causes a lowering of the ground surface elevation (Fig. 7e and f). However, after time t , the surface water gradient decreases due to the decline of ground elevation. Therefore, the sediment load drops quickly and erosion rates decline. Without subsurface flow the temporal evolution of ground surface elevation is much smoother (black dashed line in Fig. 7f).

Fig. 8 shows the spatial distribution of infiltration at steady state. The black line indicates the boundary between positive infiltration and negative infiltration (exfiltration). Upslope of this boundary, part of the precipitation infiltrates into the soil zone and moves downslope and downstream as groundwater. Downslope from this boundary the groundwater exfiltrates to the ground surface to become surface runoff. The highest infiltration rate occurs at the ridges where approximately 70% of the precipitation becomes subsurface water; the balance becomes overland flow.

The hydrologic processes evolve as the topography evolves to a steady state (Fig. 9). Initially the groundwater streamlines converge towards the catchment outlet (Fig. 9a). The magnitude of flow velocities increase towards the mid-reach of the main channel due to accumulating infiltration and recharge. The directions of groundwater flow (blue rose petals in Fig. 9e) are unimodal and the gradient magnitudes are distributed as in Fig. 9c. At steady-state, groundwater streamlines reflect local topography (Fig. 9b), the groundwater flow paths are roughly uniform distributed (yellow rose petals in Fig. 9e), and the gradient magnitudes become normal distributed (Fig. 9d).

4. Experiment 2: sensitivity of results to mesh geometry

Landscapes predicted by a LEM should not depend upon the mesh geometry (Braun and Sambridge, 1997). Here we explore the effects of mesh resolution and minimum triangle angle on a 15,000 m by 15,000 m model domain. As introduced in section 2.4, LE-PIHM uses Delaunay triangles to compose the domain mesh.

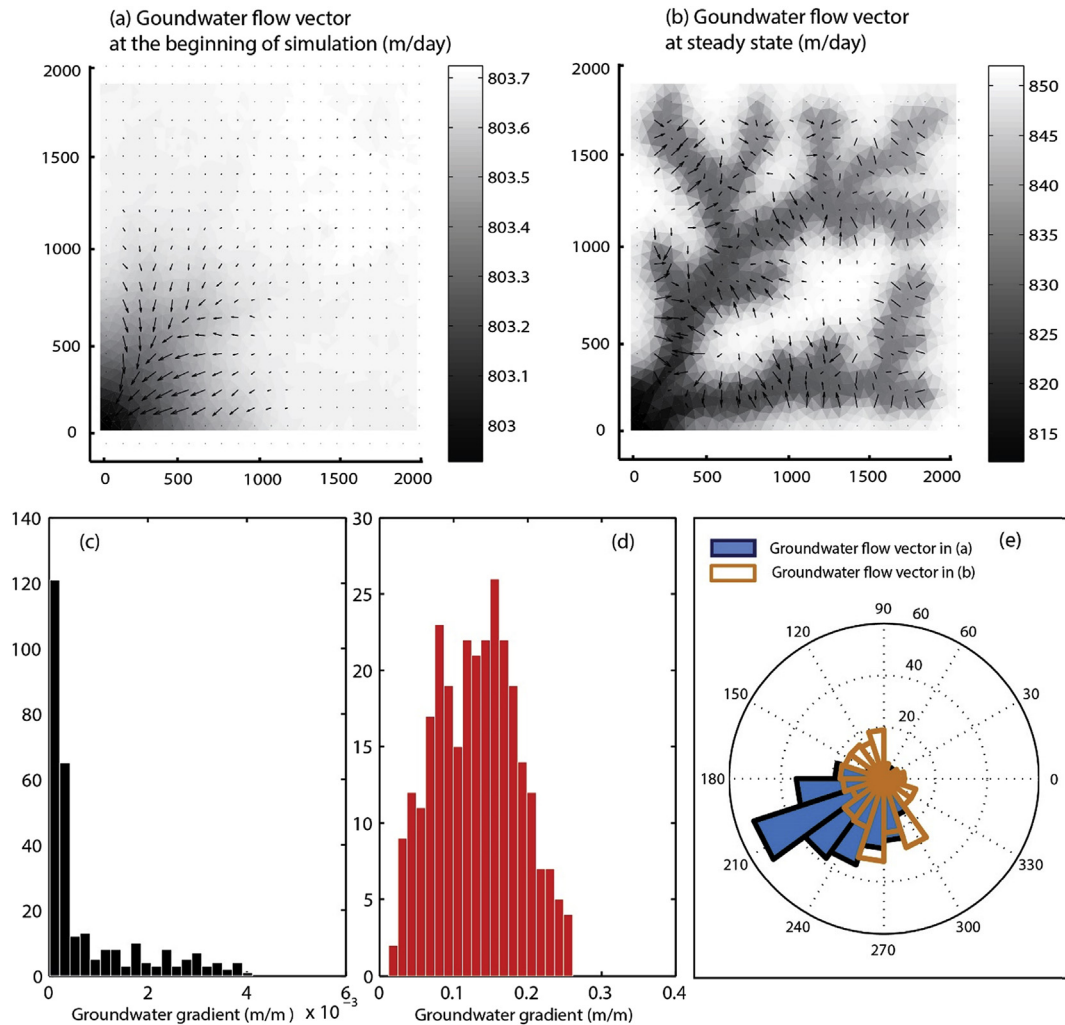


Fig. 9. Evolution of groundwater flow and distribution of groundwater gradient and flow direction at the beginning of the simulation and at steady state. (a) Surface topography (scale at right in meters) with groundwater flow vectors at the beginning of the simulation; (b) surface topography with groundwater flow vectors at steady state; (c) histogram of initial groundwater gradients (a); (d) histogram of groundwater gradients at steady-state (b); (e) distributions of groundwater flow directions at an early stage of the simulation and at steady state.

The commonly-used parameters that constrain the size and shape of the triangles are the maximum area and the minimum internal angle (Shewchuk, 1996). To explore the effect of triangle geometry on the model results we varied the maximum area allowed for an individual triangle from 250,000 to 400,000 to 500,000 m² while holding the minimum angle equal to 25°. In the second set of simulations the maximum area is held constant at 400,000 m², while the minimum angle is progressively changed from 20° to 25° to 30°.

Fig. 10 shows the predicted landscapes as a function of these cell geometries. The specific locations of the channels vary (Fig. 10, column 1), but the Hortonian coefficients of the channel network remain similar (columns 2–4). The Hortonian network coefficients vary little over the range of cell sizes used, and are similar to observed networks. The constants, b_1 , b_2 , and b_3 vary by only a few hundredths among the three cases, and the fractal dimensions of 1.94, 2.08, and 2.09 are similar and cluster around two, the value observed in nature. Likewise, the predicted landscapes are also very weakly dependent upon minimum cell interior angle. The Hortonian coefficients again cluster around expected values and the fractal dimensions are invariant and close to 2. The hypsometric

curves of elevation as a function of relative area at steady-state are also insensitive to variations in minimum cell angle and maximum cell area (Fig. 11). The group with the same maximum cell area (right) shows a better agreement than the group with the same minimum angle (left).

Although the statistics of the channel network and landscape hypsometry are nearly invariant to mesh geometry, the drainage nets show a large variation in planform. This is a result of the initial flat surface at the start of the experiments. Because the flux directions must be normal to the edges of elements, the element shapes exert a strong control on the early channel development (also see Perron and Fagherazzi, 2012).

5. Experiment 3: sensitivity of results to morphologic scale factor

From a discussion of morphologic acceleration errors by Roelvink (2006), we know that there is an optimal morphologic scale factor (MSF) for a simulation such that the MSF is large enough to accelerate the morphological process to yield an acceptable computational time but small enough to produce scale-

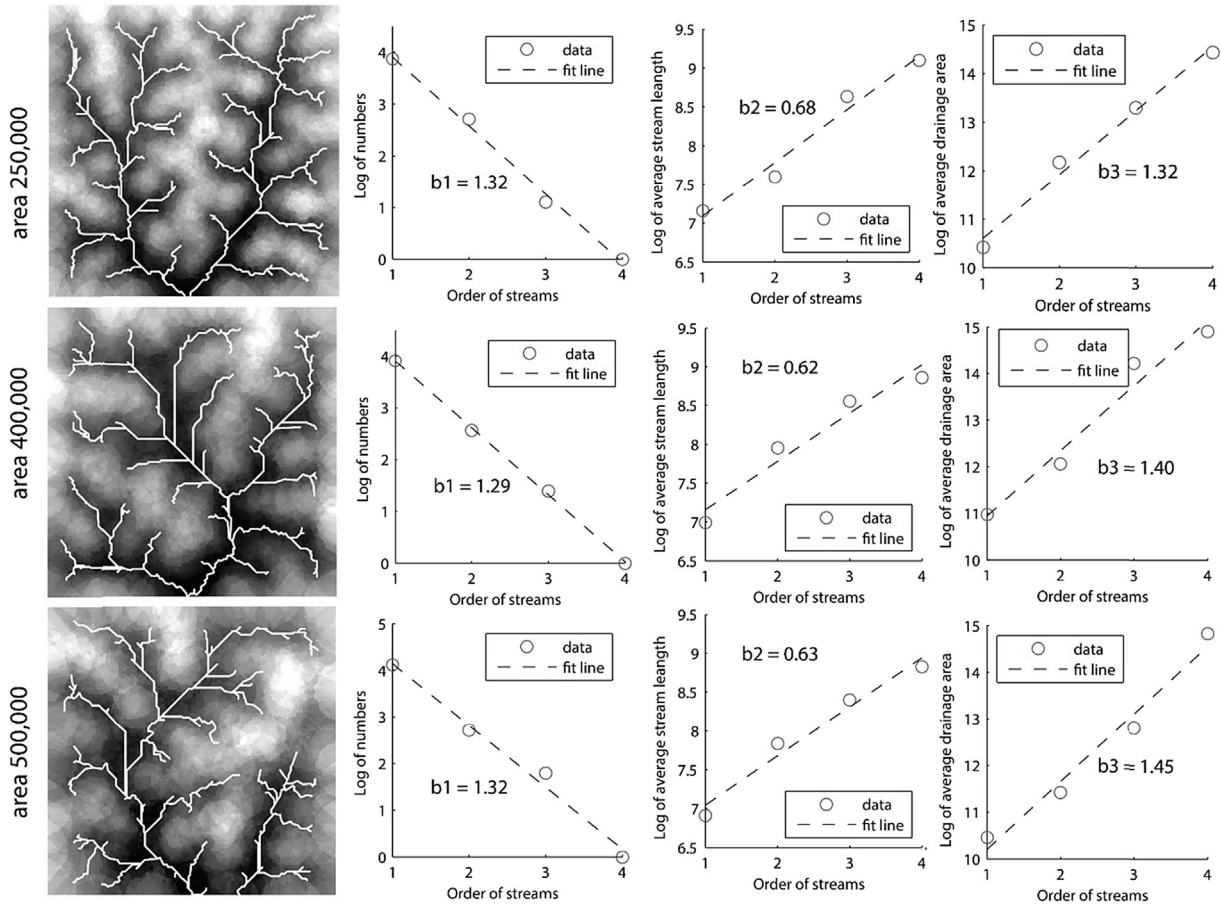


Fig. 10. Predicted landscapes for three different meshes in which the maximum area of an individual cell has been constrained. Maximum areas are 250 000 m² (top row), 400 000 m² (middle row), and 500 000 m² (bottom row). Column 1: predicted drainage nets; column 2: the number of stream reaches of a given order; column 3: average reach length of a given order; and column 4: average drainage area for each order stream. Although the location of the drainage nets change as a function of cell area, the Hortonian coefficients are relatively invariant.

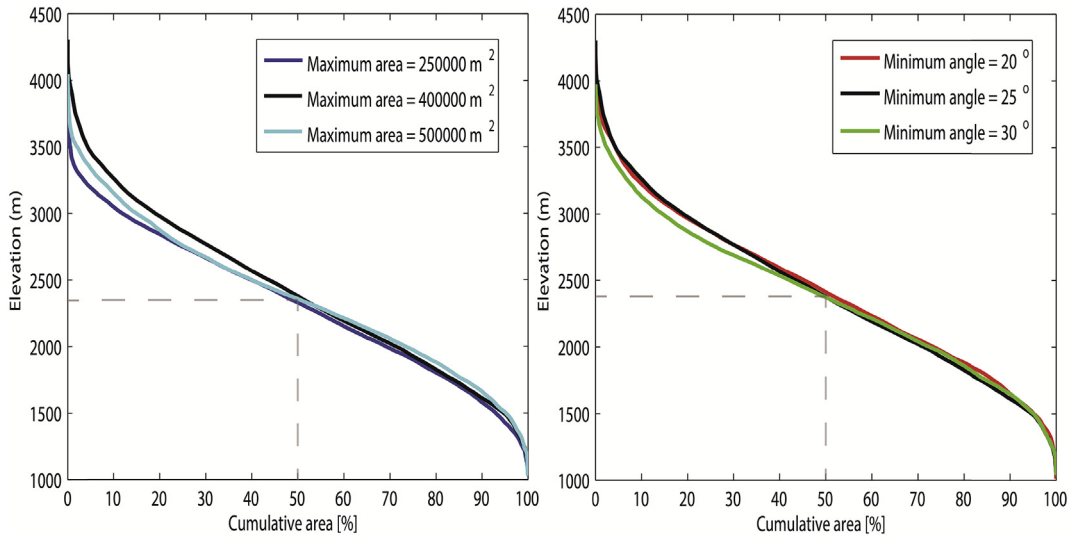


Fig. 11. Hypsometric curves of the cases with different minimum interior angle and maximum area. Left: hypsometric curves with the same minimum angle but different maximum area. Right: hypsometric curves with the same maximum area but different minimum angle. Although the plots show a difference at the top of the hypsometric curve, the value and pattern are almost invariant with different mesh structure.

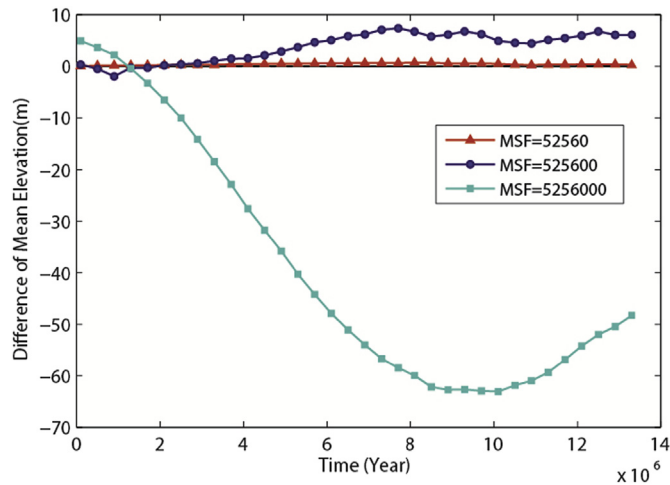


Fig. 12. Differences of the mean elevation between various MSFs and $MSF = 5256$ through time. Zero line means no difference of the mean elevation with the simulation of $MSF = 5256$.

independence of the solution. To give some guidance in this matter we simulated four landscapes using the same parameters and initial and boundary conditions, but varied the MSF. We create four simulations with a hydrologic time interval of 1 min, and MSFs equal to 5,256, 52,560, 525,600, and 5,256,000, respectively. Thus 1 min of hydrological time is corresponding to 0.01, 0.1, 1, and 10 years of morphologic time. The averaged distance between two nodes in the experiment is 170 m.

All four simulations predict a similar channel pattern, network density, and channel spacing, regardless of MSF. The simulations accelerated by MSFs of 5256 and 52,560 predict the same channel structure. The mean elevation of the landscapes at various time in the approach to steady state are shown in Fig. 12. We use the simulation with $MSF = 5256$ as a reference (0.1 year of morphological change for every hydrological minute), assuming the simulation is the most accurate we could compute within a reasonable computational time. The mean elevation of the modeled landscapes increasingly diverges from the reference mean elevation as the MFS increases.

The influence of the morphological scale factor at the element scale is presented in Fig. 13. The plots from top to bottom show the evolution of ground surface elevation at various points in the simulated landscape from upstream to downstream. In general, the trajectories for a $MSF = 5256$ and 52,560 are identical to each other. The two cases with larger MSFs show increasing disagreement. Under the initial and boundary conditions used here, it appears that a MSF of 52,560 is optimal. Model runs using smaller scale factors have infeasible computation times, and simulations with larger scale factors are inaccurate. Note that this conclusion is valid only for the case of a constant precipitation rate and the constants used in this study. Additional numerical experiments are required to establish an upper bound on the MSF for the case of variable precipitation records containing intense rainfall events.

6. Software development environment and computational time

The operating systems for executing the model are Linux, Unix, and Mac OS; the operating system for programming can be any software system. The programming language is C. The data pre-processing tool is PIHMgis available at: <http://www.pihm.psu.edu/>

pihmgis_home.html. Besides the code a user needs the SUNDIALS ODE Solver, an open source and free solver available at: <https://computation.llnl.gov/casc/sundials/main.html>. Four GB or more of RAM are needed. The computational time varies with different processors. As an example, the computational time for each simulation in this study is listed in Table 2.

7. Limitations and future work

This study simulates a two-layer landscape with a regolith layer and a bedrock layer. Subsequent versions of LE-PIHM should consider groundwater flow and solute transport in a saprolite layer (Kim et al., 2014) and a fractured bedrock layer (Rempe and Dietrich, 2014). Landslide and nonlinear creep equations will be added to the subsequent version of LE-PIHM.

This study presents the model from the modeling and software perspectives, and several synthetic experiments are conducted to test the model ability. More simulations of real watersheds and comparison with field data are needed to further explore the role of groundwater processes on landscape evolution. In order to demonstrate the optimal MSF within an acceptable computing time, experiment 3 uses a large precipitation to drive sediment erosion. From the theory perspective, experiment 3 successfully shows the stability of using MSF and how to determine an optimal MSF. But more experiments with smaller rainfall will be discussed in the future work.

8. Conclusions

We have presented a new 3-D landscape evolution model (LE-PIHM) that couples surface and subsurface hydrological processes with hillslope erosion, fluvial erosion, tectonic processes, and bedrock weathering using the semi-discrete finite volume method. A computational domain is decomposed using Delaunay triangulation. Physically-based equations are implemented to describe the impact of surface and subsurface hydrological processes on erosion. A system of 7 governing equations is assembled in each of N cells to form a system of $7 \times N$ ODEs that are solved simultaneously at each time step for surface elevation, bedrock elevation, canopy water storage, snow, surface water depth, unsaturated water storage, and saturated water storage. Particularly, the processes of groundwater seepage and groundwater sapping are well described in this model. Advantages of the model are the tight coupling of hydrologic and morphologic processes, and the ability to speed up morphologic time using a scaling factor. Several tests of the steady state landscape show that the predicted landscape matches the features of natural landscapes, and the interaction between the processes reflects the natural physical mechanisms. For example, analysis of the sediment transport rate at the outlet to a catchment shows how the sediment transport rate responds to exfiltration events, and causes changes in channel slope. The model also predicts the evolution of groundwater flow as a landscape evolves to a steady-state geometry. The importance of coupling subsurface flow is demonstrated here by comparing the steady-state landscapes with and without subsurface flow. The modeled landscape with subsurface flow possesses steeper hillslopes and higher relief. A sensitivity analysis of the model on mesh size reveals that the landscape statistics predicted by LE-PIHM are invariant to mesh geometry, giving similar network Horton statistics and hypsometric curves of elevation. A morphological acceleration technique is introduced and the method of choosing optimal morphological scale factor is provided. We emphasized the importance of the stability of the co-evolution system (hydrological-morphological system) by conducting experiment 3 with different MSF. As shown in experiment 3, even if a large morphological time step, like 1 year or 10 year, is

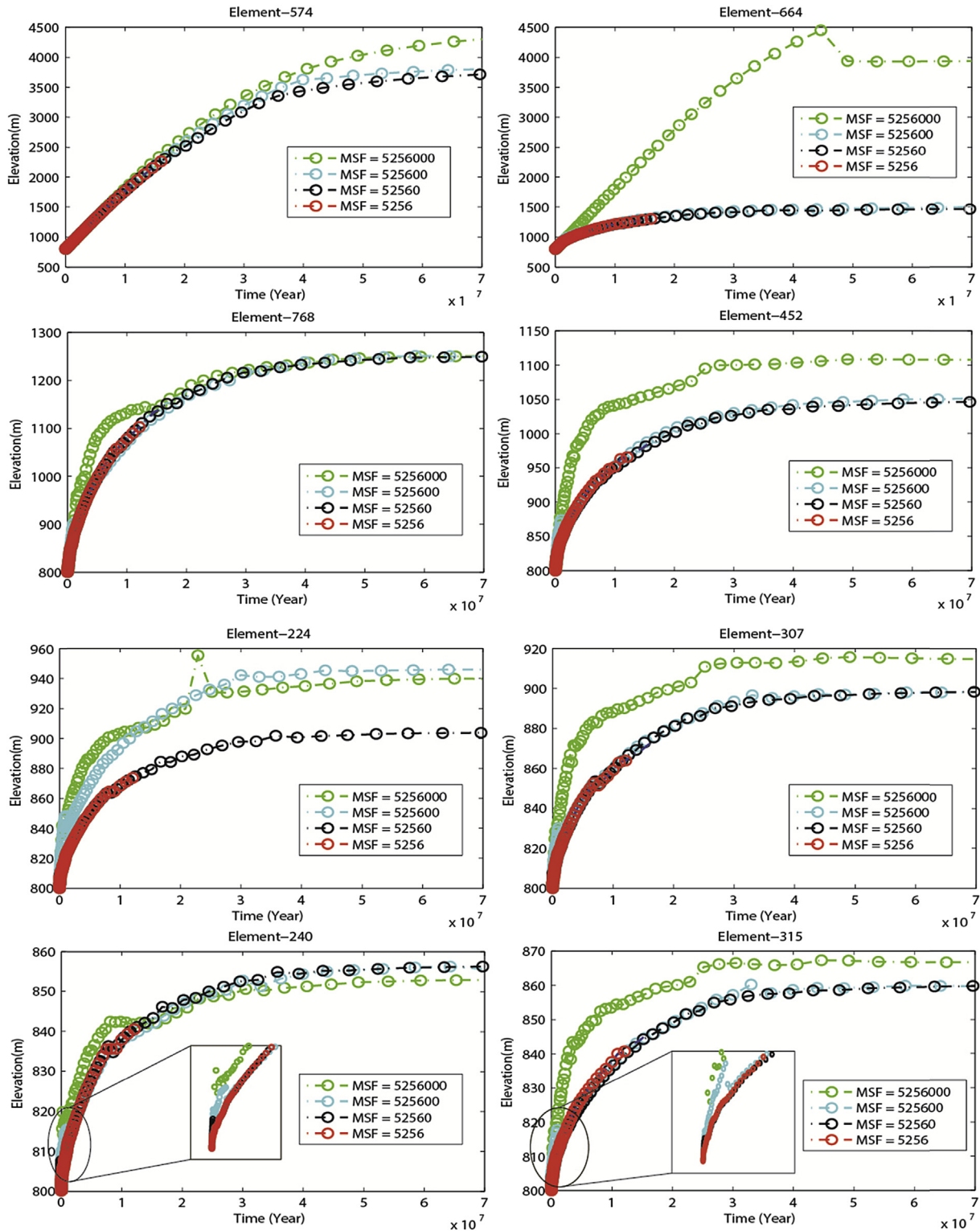


Fig. 13. Element scale comparison of the evolution of the ground elevation of the elements. The plots from top to bottom represent the elements from upstream to downstream. The five plots in the left column are the samples of elements along the left channel tributary. The five plots in the right column collect the samples of elements along the right tributary. The two inset plots within the bottom two plots are the amplified view of the elevation change at the beginning of the simulation. The cases of MSF = 5256 and 52,560 show a very similar pattern.

numerically stable for the morphological processes (Courant–Friedrichs–Lewy condition), the original interaction between morphological and hydrological processes changes during the evolution processes.

Landslide and nonlinear creep equations will be added to the subsequent version of LE-PIHM. Simulating groundwater and solute transport in weathered bedrock and fractured bedrock layer will be considered as well.

Acknowledgments

Thanks for the constructive comments from the three anonymous reviewers. This work was facilitated by NSF Critical Zone Observatory program grants to CJD (EAR 07-25019) and SLB (EAR 12-39285, EAR 13-31726). This research was conducted in Penn State's Stone Valley Forest, which is supported and managed by the Penn State's Forestland Management Office in the College of Agricultural Sciences. Student research grant from the Geological Society of America also provides partial support for this research. Author contributions: Y.Z. and R.S. designed the research; Y.Z. performed the research and analyzed the data; C.D. provided support on hydrological analysis and PIHM model integration, and Y.Z., R.S. and C.D. wrote the paper.

References

- Abrams, D.M., Lobkovsky, A.E., Petroff, A.P., Straub, K.M., McElroy, B., Mohrig, D.C., Kudrolli, A., Rothman, D.H., 2009. Growth laws for channel networks incised by groundwater flow. *Nat. Geosci.* 2 (3), 193–196.
- Ahnert, F., 1977. Some comments on the quantitative formulation of geomorphological processes in a theoretical model. *Earth Surf. Process.* 2 (2–3), 191–201.
- Anderson, R.S., 2002. Modeling the tor-dotted crests, bedrock edges, and parabolic profiles of high alpine surfaces of the Wind River Range, Wyoming. *Geomorphology* 46 (1), 35–58.
- Anderson, S.P., Bales, R.C., Duffy, C.J., 2008. Critical zone observatories: building a network to advance interdisciplinary study of Earth surface processes. *Mineral. Mag.* 72 (1), 7–10.
- Andrews, D., Bucknam, R.C., 1987. Fitting degradation of shoreline scarps by a nonlinear diffusion model (1978–2012). *J. Geophys. Res. Solid Earth* 92 (B12), 12857–12867.
- Armson, K., Fessenden, R., 1973. Forest windthrows and their influence on soil morphology. *Soil Sci. Soc. Am. J.* 37 (5), 781–783.
- Aubertin, G.M., 1971. Nature and Extent of Macropores in Forest Soils and Their Influence on Subsurface Water Movement. Northeastern Forest Experiment Station.
- Baker, G., 1915. A windfall problem. *J. For.* 13 (3), 317–324.
- Barkwith, A., Hurst, M.D., Jackson, C.R., Wang, L., Ellis, M.A., Coulthard, T.J., 2015. Simulating the influences of groundwater on regional geomorphology using a distributed, dynamic, landscape evolution modelling platform. *Environ. Model. Softw.* 74, 1–20.
- Beaumont, C., Kooi, H., Willett, S., 2000. Coupled tectonic-surface process models with applications to rifted margins and collisional orogens. *Geomorphol. Glob. Tect.* 29–55.
- Beven, K., Germann, P., 1982. Macropores and water flow in soils. *Water Resour. Res.* 18 (5), 1311–1325.
- Beven, K., Germann, P., 2013. Macropores and water flow in soils revisited. *Water Resour. Res.* 49 (6), 3071–3092.
- Bhatt, G., Kumar, M., Duffy, C.J., 2014. A tightly coupled GIS and distributed hydrologic modeling framework. *Environ. Model. Softw.* 62, 70–84.
- Bishop, P., 2007. Long-term landscape evolution: linking tectonics and surface processes. *Earth Surf. Process. Landforms* 32 (3), 329–365.
- Bouma, J., 1981. Soil morphology and preferential flow along macropores. *Agric. Water Manag.* 3 (4), 235–250.
- Brantley, S.L., Goldhaber, M.B., Ragnarsdottir, K.V., 2007. Crossing disciplines and scales to understand the critical zone. *Elements* 3 (5), 307–314.
- Bras, R.L., 1990. *Hydrology: an Introduction to Hydrologic Science*. Addison-Wesley Reading.
- Braun, J., Sambridge, M., 1997. Modelling landscape evolution on geological time scales: a new method based on irregular spatial discretization. *Basin Res.* 9 (1), 27–52.
- Byrne, G.D., 1992. Pragmatic experiments with Krylov methods in the stiff ODE setting. Institute Of Mathematics and its Applications Conference Series. Oxford University Press, pp. 323–323.
- Cohen, S., Willgoose, G., Hancock, G., 2010. The mARM3D spatially distributed soil evolution model: three-dimensional model framework and analysis of hillslope and landform responses (2003–2012). *J. Geophys. Res. Earth Surf.* (F4), 115.
- Cohen, S.D., Hindmarsh, A.C., 1996. CVODE, a stiff/nonstiff ODE solver in C. *Comput. Phys.* 10 (2), 138–143.
- Coulthard, T., Kirkby, M., Macklin, M., 2000. Modelling geomorphic response to environmental change in an upland catchment. *Hydrol. Process.* 14 (11–12), 2031–2045.
- Coulthard, T.J., 2001. Landscape evolution models: a software review. *Hydrol. Process.* 15 (1), 165–173.
- Culling, W., 1963. Soil creep and the development of hillside slopes. *J. Geol.* 71 (2), 127–161.
- Davison, C., 1889. IV.—On the creeping of the soilcap through the action of frost. *Geol. Mag. (Decade III)* 6 (06), 255–261.
- Dietrich, W.E., Bellugi, D.G., Sklar, L.S., Stock, J.D., Heimsath, A.M., Roering, J.J., 2003. Geomorphic transport laws for predicting landscape form and dynamics. *Predict. Geomorphol.* 103–132.
- Dietrich, W.E., Perron, J.T., 2006. The search for a topographic signature of life. *Nature* 439 (7075), 411–418.
- Faeh, A.O., Scherrer, S., Naef, F., 1997. A combined field and numerical approach to investigate flow processes in natural macroporous soils under extreme precipitation. *Hydrol. Earth Syst. Sci. Discuss.* 1 (4), 787–800.
- Fox, G.A., Wilson, G.V., Simon, A., Langendoen, E.J., Akay, O., Fuchs, J.W., 2007. Measuring streambank erosion due to ground water seepage: correlation to bank pore water pressure, precipitation and stream stage. *Earth Surf. Process. Landforms* 32 (10), 1558–1573.
- Francipane, A., Ivanov, V.Y., Noto, L.V., Istanbuloglu, E., Arnone, E., Bras, R.L., 2012. tRIBS-Erosion: a parsimonious physically-based model for studying catchment hydro-geomorphic response. *Catena* 92, 216–231.
- Furbish, D.J., Haff, P.K., Dietrich, W.E., Heimsath, A.M., 2009. Statistical description of slope-dependent soil transport and the diffusion-like coefficient (2003–2012). *J. Geophys. Res. Earth Surf.* (F3), 114.
- Gabet, E.J., 2000. Gopher bioturbation: field evidence for non-linear hillslope diffusion. *Earth Surf. Process. Landforms* 25 (13), 1419–1428.
- Gabet, E.J., 2003. Sediment transport by dry ravel (1978–2012). *J. Geophys. Res. Solid Earth* (B1), 108.
- Gabet, E.J., Mudd, S.M., 2010. Bedrock erosion by root fracture and tree throw: a coupled biogeomorphic model to explore the humped soil production function and the persistence of hillslope soils (2003–2012). *J. Geophys. Res. Earth Surf.* (F4), 115.
- Gabet, E.J., Reichman, O., Seabloom, E.W., 2003. The effects of bioturbation on soil processes and sediment transport. *Annu. Rev. Earth Planet. Sci.* 31 (1), 249–273.
- George, D.A., Gelfenbaum, G., Stevens, A.W., 2012. Modeling the hydrodynamic and morphologic response of an estuary restoration. *Estuaries Coasts* 35 (6), 1510–1529.
- Gilbert, G., 1877. Report on the Geology of the Henry Mountains: US Geographical and Geological Survey. Rocky Mountain Region.
- Gilbert, G.K., Dutton, C.E., 1880. Report on the Geology of the Henry Mountains. US Government Printing Office.
- Gottardi, G., Venutelli, M., 1993. A control-volume finite-element model for two-dimensional overland flow. *Adv. Water Resour.* 16 (5), 277–284.
- Heimsath, A.M., Chappell, J., Dietrich, W.E., Nishiizumi, K., Finkel, R.C., 2000. Soil production on a retreating escarpment in southeastern Australia. *Geology* 28 (9), 787–790.
- Heimsath, A.M., Chappell, J., Dietrich, W.E., Nishiizumi, K., Finkel, R.C., 2001. Late Quaternary erosion in southeastern Australia: a field example using cosmogenic nuclides. *Quat. Int.* 83, 169–185.
- Heimsath, A.M., Dietrich, W.E., Nishiizumi, K., Finkel, R.C., 1997. The soil production function and landscape equilibrium. *Nature* 388 (6640), 358–361.
- Heimsath, A.M., Fink, D., Hancock, G.R., 2009. The 'humped' soil production function: eroding Arnhem Land, Australia. *Earth Surf. Process. Landforms* 34 (12), 1674–1684.
- Hellmer, M.C., Rios, B.A., Ouimet, W.B., Sibley, T.R., 2015. Ice storms, tree throw, and hillslope sediment transport in northern hardwood forests. *Earth Surf. Process. Landf.* 40 (7), 901–912.
- Higgins, C.G., 1982. Drainage systems developed by sapping on Earth and Mars. *Geology* 10 (3), 147–152.
- Horton, R.E., 1945. Erosional development of streams and their drainage basins; hydrophysical approach to quantitative morphology. *Geol. Soc. Am. Bull.* 56 (3), 275–370.
- Howard, A.D., 1988. Groundwater sapping experiments and modeling. *Sapping Featur. Colo. Plateau A Comp. Planet. Geol. Field Guide* 491, 71–83.
- Howard, A.D., 1994. A detachment-limited model of drainage basin evolution. *Water Resour. Res.* 30 (7), 2261–2285.
- Istanbuloglu, E., Bras, R.L., 2005. Vegetation-modulated landscape evolution: effects of vegetation on landscape processes, drainage density, and topography (2003–2012). *J. Geophys. Res. Earth Surf.* (F2), 110.
- Jones, J.E., Woodward, C.S., 2001. Newton–Krylov–multigrid solvers for large-scale, highly heterogeneous, variably saturated flow problems. *Adv. Water Res.* 24 (7), 763–774.
- Kim, H., Bishop, J.K., Dietrich, W.E., Fung, I.Y., 2014. Process dominance shift in solute chemistry as revealed by long-term high-frequency water chemistry observations of groundwater flowing through weathered argillite underlying a steep forested hillslope. *Geochim. Cosmochim. Acta* 140, 1–19.
- Kirkby, M., 1967. Measurement and theory of soil creep. *J. Geol.* 359–378.
- Kochel, R., Howard, A., McLane, C., 1985. Channel networks developed by groundwater sapping in fine-grained sediments: analogs to some Martian valleys. *Models Geomorphol.* 313–341.
- Kumar, M., 2009. *Toward a Hydrologic Modeling System*. Department of Civil and Environmental Engineering, The Pennsylvania State University, p. 273.
- Laity, J.E., Malin, M.C., 1985. Sapping processes and the development of theater-headed valley networks on the Colorado Plateau. *Geol. Soc. Am. Bull.* 96 (2), 203–217.
- Lamb, M.P., Dietrich, W.E., Aciego, S.M., DePaolo, D.J., Manga, M., 2008. Formation of box canyon, Idaho, by megaflood: implications for seepage erosion on earth and mars. *Science* 320 (5879), 1067–1070.
- Lesser, G., Roelvink, J., Van Kester, J., Stelling, G., 2004. Development and validation of a three-dimensional morphological model. *Coast. Eng.* 51 (8), 883–915.
- Lobkovsky, A.E., Smith, B.E., Kudrolli, A., Mohrig, D.C., Rothman, D.H., 2007. Erosive dynamics of channels incised by subsurface water flow (2003–2012). *J. Geophys. Res. Earth Surf.* (F3), 112.

- Martin, Y., Church, M., 1997. Diffusion in landscape development models: on the nature of basic transport relations. *Earth Surf. Process. Landforms* 22 (3), 273–279.
- Martin, Y., Church, M., 2004. Numerical modelling of landscape evolution: geomorphological perspectives. *Prog. Phys. Geogr.* 28 (3), 317–339.
- Matsuoka, N., 1998. Modelling frost creep rates in an alpine environment. *Permafrost. Periglacial Process.* 9 (4), 397–409.
- McNamara, J.P., Ziegler, A.D., Wood, S.H., Vogler, J.B., 2006. Channel head locations with respect to geomorphologic thresholds derived from a digital elevation model: a case study in northern Thailand. *For. Ecol. Manag.* 224 (1), 147–156.
- Miller, S.R., Sak, P.B., Kirby, E., Bierman, P.R., 2013. Neogene rejuvenation of central Appalachian topography: evidence for differential rock uplift from stream profiles and erosion rates. *Earth Planet. Sci. Lett.* 369, 1–12.
- Minasny, B., Finke, P., Stockmann, U., Vanwallegem, T., McBratney, A.B., 2015. Resolving the integral connection between pedogenesis and landscape evolution. *Earth-Science Rev.* 150, 102–120.
- Norman, S.A., Schaeztl, R.J., Small, T.W., 1995. Effects of slope angle on mass movement by tree uprooting. *Geomorphology* 14 (1), 19–27.
- Paik, K., 2012. Simulation of landscape evolution using a global flow path search method. *Environ. Model. Softw.* 33, 35–47.
- Parker, G., Toro-Escobar, C.M., Ramey, M., Beck, S., 2003. Effect of floodwater extraction on mountain stream morphology. *J. Hydraulic Eng.* 129 (11), 885–895.
- Perron, J.T., Dietrich, W.E., Kirchner, J.W., 2008. Controls on the spacing of first-order valleys (2003–2012). *J. Geophys. Res. Earth Surf. (F4)*, 113.
- Perron, J.T., Fagherazzi, S., 2012. The legacy of initial conditions in landscape evolution. *Earth Surf. Process. Landforms* 37 (1), 52–63.
- Perron, J.T., Richardson, P.W., Ferrier, K.L., Lapôtre, M., 2012. The root of branching river networks. *Nature* 492 (7427), 100–103.
- Petroff, A.P., Devauchelle, O., Abrams, D.M., Lobkovsky, A.E., Kudrolli, A., Rothman, D.H., 2011. Geometry of valley growth. *J. Fluid Mech.* 673, 245–254.
- Petroff, A.P., Devauchelle, O., Kudrolli, A., Rothman, D.H., 2012. Four remarks on the growth of channel networks. *Comptes Rendus Geosci.* 344 (1), 33–40.
- Petroff, A.P., Devauchelle, O., Seybold, H., Rothman, D.H., 2013. Bifurcation dynamics of natural drainage networks. *Philosophical Trans. R. Soc. A Math. Phys. Eng. Sci.* 371 (2004), 20120365.
- Prosser, I.P., Rustomji, P., 2000. Sediment transport capacity relations for overland flow. *Prog. Phys. Geogr.* 24 (2), 179–193.
- Qu, Y., Duffy, C.J., 2007. A semidiscrete finite volume formulation for multiprocess watershed simulation. *Water Resour. Res.* 43 (8) n/a–n/a.
- Rempe, D.M., Dietrich, W.E., 2014. A bottom-up control on fresh-bedrock topography under landscapes. *Proc. Natl. Acad. Sci.* 201404763.
- Rodriguez-Iturbe, I., Rinaldo, A., 2001. *Fractal river basins: chance and self-organization*. Cambridge University Press.
- Roelvink, J., 2006. Coastal morphodynamic evolution techniques. *Coast. Eng.* 53 (2), 277–287.
- Roering, J.J., 2008. How well can hillslope evolution models “explain” topography? Simulating soil transport and production with high-resolution topographic data. *Geol. Soc. Am. Bull.* 120 (9–10), 1248–1262.
- Roering, J.J., Gerber, M., 2005. Fire and the evolution of steep, soil-mantled landscapes. *Geology* 33 (5), 349–352.
- Roering, J.J., Kirchner, J.W., Dietrich, W.E., 1999. Evidence for nonlinear, diffusive sediment transport on hillslopes and implications for landscape morphology. *Water Resour. Res.* 35 (3), 853–870.
- Roering, J.J., Kirchner, J.W., Dietrich, W.E., 2001. Hillslope evolution by nonlinear, slope-dependent transport: steady state morphology and equilibrium adjustment timescales (1978–2012). *J. Geophys. Res. Solid Earth* 106 (B8), 16499–16513.
- Roering, J.J., Marshall, J., Booth, A.M., Mort, M., Jin, Q., 2010. Evidence for biotic controls on topography and soil production. *Earth Planet. Sci. Lett.* 298 (1), 183–190.
- Ruel, J.-C., 2000. Factors influencing windthrow in balsam fir forests: from landscape studies to individual tree studies. *For. Ecol. Manag.* 135 (1), 169–178.
- Schaeztl, R.J., Johnson, D.L., Burns, S.F., Small, T.W., 1989. Tree uprooting: review of terminology, process, and environmental implications. *Can. J. For. Res.* 19 (1), 1–11.
- Scheidegger, A., 1961. Mathematical models of slope development. *Geol. Soc. Am. Bull.* 72 (1), 37–50.
- Schumm, S., Boyd, K., Wolff, C., Spitz, W., 1995. A ground-water sapping landscape in the Florida Panhandle. *Geomorphology* 12 (4), 281–297.
- Schumm, S.A., 1956. Evolution of drainage systems and slopes in badlands at Perth Amboy, New Jersey. *Geol. Soc. Am. Bull.* 67 (5), 597–646.
- Sharp, R.P., 1982. Landscape evolution (a review). *Proc. Natl. Acad. Sci. U. S. A.* 79, 4477–4486.
- Shewchuk, J.R., 1996. Triangle: Engineering a 2D Quality Mesh Generator and Delaunay Triangulator. In: *Applied Computational Geometry towards Geometric Engineering*. Springer, pp. 203–222.
- Small, E.E., Anderson, R.S., Hancock, G.S., 1999. Estimates of the rate of regolith production using ¹⁰Be and ²⁶Al from an alpine hillslope. *Geomorphology* 27 (1), 131–150.
- Tarboton, D.G., Bras, R.L., Rodriguez-Iturbe, I., 1988. The fractal nature of river networks. *Water Resour. Res.* 24 (8), 1317–1322.
- Teng, S.-H., Wong, C.W., 2000. Unstructured mesh generation: theory, practice, and perspectives. *Int. J. Comput. Geometry Appl.* 10 (03), 227–266.
- Thomas, G.W., Phillips, R.E., 1979. Consequences of water movement in macropores. *J. Environ. Qual.* 8 (2), 149–152.
- Tucker, G., Lancaster, S., Gasparini, N., Bras, R., 2001. The Channel-hillslope Integrated Landscape Development Model (CHILD). In: *Landscape Erosion and Evolution Modeling*. Springer, pp. 349–388.
- Tucker, G.E., Bras, R.L., 1998. Hillslope processes, drainage density, and landscape morphology. *Water Resour. Res.* 34 (10), 2751–2764.
- Tucker, G.E., Hancock, G.R., 2010. Modelling landscape evolution. *Earth Surf. Process. Landforms* 35 (1), 28–50.
- Tucker, G.E., Slingerland, R.L., 1994. Erosional dynamics, flexural isostasy, and long-lived escarpments: a numerical modeling study (1978–2012). *J. Geophys. Res. Solid Earth* 99 (B6), 12229–12243.
- Ulanova, N.G., 2000. The effects of windthrow on forests at different spatial scales: a review. *For. Ecol. Manag.* 135 (1), 155–167.
- Van der Wegen, M., Roelvink, J., 2008. Long-term morphodynamic evolution of a tidal embayment using a two-dimensional, process-based model. *J. Geophys. Res. Oceans (C3)*, 113, 1978–2012.
- Van Genuchten, M.T., 1980. A closed-form equation for predicting the hydraulic conductivity of unsaturated soils. *Soil Sci. Soc. Am. J.* 44 (5), 892–898.
- Warner, J.C., Sherwood, C.R., Signell, R.P., Harris, C.K., Arango, H.G., 2008. Development of a three-dimensional, regional, coupled wave, current, and sediment-transport model. *Comput. Geosciences* 34 (10), 1284–1306.
- Weiler, M., Naef, F., 2003. Simulating surface and subsurface initiation of macropore flow. *J. Hydrol.* 273 (1), 139–154.
- West, N., Kirby, E., Bierman, P., Slingerland, R., Ma, L., Rood, D., Brantley, S., 2013. Regolith production and transport at the susquehanna shale hills critical zone observatory, Part 2: insights from meteoric ¹⁰Be. *J. Geophys. Res. Earth Surf.* 118 (3), 1877–1896.
- Willett, S.D., McCoy, S.W., Perron, J.T., Goren, L., Chen, C.-Y., 2014. Dynamic reorganization of river basins. *Science* 343 (6175), 1248765.
- Willgoose, G., Bras, R.L., Rodriguez-Iturbe, I., 1991. A coupled channel network growth and hillslope evolution model: 1. Theory. *Water Resour. Res.* 27 (7), 1671–1684.
- Wong, M., Parker, G., 2006. Reanalysis and correction of bed-load relation of Meyer-Peter and Müller using their own database. *J. Hydraulic Eng.* 132 (11), 1159–1168.